

1     **Impacts of aerosol-radiation interaction on meteorological forecast**  
2     **over northern China by offline coupling the WRF-Chem simulated**  
3     **AOD into WRF: a case study during a heavy pollution event**

4

5             Yang Yang<sup>1</sup>, Min Chen<sup>1</sup>, Xiujuan Zhao<sup>1\*</sup>, Dan Chen<sup>1\*</sup>, Shuiyong Fan<sup>1</sup>,

6                             Jianping Guo<sup>2</sup>, and Shaukat Ali<sup>3</sup>

7     *1 Institute of Urban Meteorology, China Meteorological Administration, Beijing*

8                             *100089, China*

9     *2 State Key Laboratory of Severe Weather, Chinese Academy of Meteorological*

10                             *Sciences, Beijing, 100081, China*

11     *3 Global Change Impact Studies Centre, Ministry of Climate Change, Islamabad*

12                             *44000, Pakistan*

## Abstract

13  
14 To facilitate the future inclusion of aerosol-radiation interactions in the regional  
15 operational Numerical Weather Prediction (NWP) system – RMAPS-ST (adapted  
16 from Weather Research and Forecasting, WRF) at the Institute of Urban  
17 Meteorology (IUM), China Meteorological Administration (CMA), the impacts of  
18 aerosol-radiation interactions on the forecast of surface radiation and meteorological  
19 parameters during a heavy pollution event (December 6<sup>th</sup> -10<sup>th</sup>, 2015) over northern  
20 China were investigated. The aerosol information was simulated by RMAPS-Chem  
21 (adapted from WRF model coupled with Chemistry, WRF-Chem) and then  
22 offline-coupled into Rapid Radiative Transfer Model for General Circulation Models  
23 (RRTMG) radiation scheme of WRF to enable the aerosol-radiation feedback in the  
24 forecast. To ensure the accuracy of high-frequency (hourly) updated aerosol optical  
25 depth (AOD) field, the temporal and spatial variations of simulated AOD and  
26 aerosol extinction coefficient at 550nm were evaluated against in-situ and satellite  
27 observations. Comparisons with in-situ and Moderate Resolution Imaging  
28 Spectroradiometer (MODIS), AErosol Robotic NETwork (AERONET), and  
29 Cloud-Aerosol Lidar and Infrared Pathfinder Satellite Observation (CALIPSO)  
30 satellite observations showed that the model could reproduce and spatial and vertical  
31 distribution as well as the temporal variation the of polluted episode. Further  
32 comparison of PM<sub>2.5</sub> with in-situ observation showed WRF-Chem reasonably  
33 captured the PM<sub>2.5</sub> field in terms of spatial distribution and magnitude, with the

34 correlation coefficients of 0.85, 0.89, 0.76, 0.92 and 0.77 at Beijing, Shijiazhuang,  
35 Tianjin, Hebei and Henan, respectively. Forecasts with/without the aerosol  
36 information were conducted further, and the differences of surface radiation, energy  
37 budget, and meteorological parameters were evaluated against surface and sounding  
38 observations. The offline-coupling simulation (with aerosol-radiation interaction  
39 active) showed a remarkable decrease of downward shortwave (SW) radiation  
40 reaching surface, thus helping to reduce the overestimated SW radiation during  
41 daytime. The simulated surface radiation budget was also improved, with the biases  
42 of net surface radiation decreased by 85.3%, 50.0%, 35.4%, and 44.1% during  
43 daytime at Beijing, Tianjin, Taiyuan and Jinan respectively, accompanied by the  
44 reduction of sensible ( $16.1 \text{ W m}^{-2}$ , 18.5%) and latent ( $6.8 \text{ W m}^{-2}$ , 13.4%) heat fluxes  
45 emitted by the surface at noon-time. In addition, the cooling of 2-m temperature  
46 ( $\sim 0.40 \text{ }^\circ\text{C}$ ) and the decrease of horizontal wind speed near surface ( $\sim 0.08 \text{ m s}^{-1}$ )  
47 caused by the aerosol-radiation interaction over northern China helped to reduce the  
48 bias by  $\sim 73.9\%$  and  $\sim 7.8\%$  respectively, particularly during daytime. Further  
49 comparisons indicated that the simulation implemented AOD could better capture  
50 the vertical structure of atmospheric wind. Accompanied with the lower planetary  
51 boundary layer and the increased atmospheric stability, both U and V wind at  
52 850hPa showed the convergence which were unfavorable for pollutants dispersion.  
53 Since RMPAS-ST provides meteorological initial condition for RMAPS-Chem, the  
54 changes of meteorology introduced by aerosol-radiation interaction would routinely

55 impact the simulations of pollutants. To verify the statistically significance of the  
56 results, we further conducted the 24-hour forecasts for a longer period lasting 27  
57 days (Jan. 13<sup>th</sup> – Feb. 8<sup>th</sup>, 2017), with no AOD field (NoAero) and WRF-Chem  
58 simulated hourly AOD fields (Aero) included, as well as constant AOD value of  
59 0.12 (ClimAero), respectively. The one-month results were statistically significant  
60 and indicated that the mean RMSE of 2-m temperature (wind speed at 10m) in Aero  
61 and ClimAero relative to NoAero was reduced by 4.0% (1.9%) and 1.2% (1.6%).  
62 More detailed evaluations and analysis will be addressed in a future article. These  
63 results demonstrated the influence of aerosol-radiation interactions on the  
64 improvement of predictive accuracy and the potential prospects to offline couple  
65 near-real-time aerosol information in regional RMAPS-ST NWP in northern China.  
66 **Key words:** Aerosol-radiation interactions, offline-coupling, WRF, northern China,  
67 pollution

## 68 **1. Introduction**

69 Aerosol-radiation interactions modify the radiative energy budget of the  
70 earth-atmosphere system through the interaction between aerosols and solar radiation  
71 by scattering and absorbing mechanism as well as the absorption and emitting of  
72 thermal radiation (Ramanathan et al., 2001; Yu et al., 2006). The aerosol-radiation  
73 interaction may cool or heat the earth-atmosphere system, alter surface and  
74 atmospheric radiation and temperature structure on regional and global climate, which  
75 have been widely reported and studied (Hansen et al., 1997; Ramanathan et al., 2001;  
76 Kaufman et al., 2002; Liao et al., 2006; Zhang et al., 2010; Ghan et al., 2012; Yang et  
77 al., 2017a). Considering the lifetime of most aerosol particles and their locally uneven  
78 distribution, as well as their high dependence on emission sources and local  
79 meteorological conditions for dispersion (Rodwell and Jung, 2008; Liu et al., 2012;  
80 Liao et al., 2015), the impacts of episodic aerosol events over regional areas are  
81 worthy of more concerns (Cheng et al., 2017; Zheng et al., 2019).

82 With substantial aerosol loading, aerosol particles have significant influences on  
83 meteorology, and many endeavors by both field experiments and numerical models  
84 have been devoted to study the impacts of aerosol-radiation interaction on  
85 meteorological fields, including surface solar radiation, planetary boundary layer  
86 (PBL), atmospheric heating rate, atmospheric stability (Hansen et al., 1997; Ackerman  
87 et al., 2000; Quan et al., 2014; Yang et al., 2017b; Wang et al., 2018), cloud formation  
88 due to thermodynamic changes, and further the onset or reduction of precipitation

89 systems (Grell et al., 2011; Guo et al., 2016, Jiang et al., 2017). For instance, in  
90 worldwide, the simulations with Weather Research and Forecasting (WRF) model  
91 coupled with Chemistry (WRF-Chem) showed that by purely taking into account the  
92 aerosol-radiation interactions, aerosols may reduce incoming solar radiation by up to  
93 -9% (-16%) and 2-m temperatures by up to 0.16°C (0.37°C) in January (July) over  
94 the continental U.S. (Zhang et al., 2010) , affect meso-scale convection system owing  
95 to thermodynamic changes over Atlantic Ocean during Saharan dust eruption period  
96 (Chen et al., 2017), and lead to the distinct changes in precipitation due to the changes  
97 in temperature profile and stabilities induced by the aerosol-radiation interaction over  
98 Eastern China (Huang et al., 2016).

99 Northern China is experiencing heavy air pollution in past two decades, with  
100 particle matter (PM) being the primary pollutant, particularly during wintertime (Chan  
101 and Yao, 2008; Zhang et al., 2015; Zhao et al., 2019) due to the combination of high  
102 primary and precursor emissions and frequent stable meteorological conditions in this  
103 area (Elser et al., 2016; Zhang et al, 2018). The effects of aerosol-radiation interaction  
104 on meteorology were expected to be much more significant over northern China.  
105 Applying WRF and Community Multi-scale Air Quality Model (CMAQ) system  
106 (WRF-CMAQ), Wang et al. (2014) and Sekiguchi et al. (2018) reported a 53%  
107 reduction in solar radiation reaching surface and ~100m decrease of planetary  
108 boundary layer height (PBLH) in response to the presence of aerosols during a severe  
109 winter haze episode in China. Wang et al. (2015a, b) used the online chemical weather

110 forecasting mode Global/Regional Assimilation and PrEdiction System/ Chinese  
111 Unified Atmospheric Chemistry Environment (GRAPES/CUACE) and illustrated that  
112 the solar radiation at ground decreased by 15% in Beijing–TianJin–Hebei, China, and  
113 its near surroundings, accompanied by the decrease in turbulence diffusion of about  
114 52% and a decrease in PBLH of about 33 % during a haze episode of summertime in  
115 2008.

116       Considering the significant influence of the aerosol-radiation interaction on  
117 meteorological forecasts as illustrated in many studies (Kaufman et al., 2002; Zhang  
118 et al., 2010), several weather forecast centers are conducting research to facilitate the  
119 inclusion of more complex aerosol information in operational numerical weather  
120 prediction (NWP) models. For example, Rodwell and Jung (2008) showed the local  
121 medium-range forecast skills were improved due to the application of new  
122 climatological aerosol distribution in European Centre for Medium-Range Weather  
123 Forecasts (ECMWF). Recently, a positive impact up to a 48h lead time on the 2m  
124 temperature and forecasts of surface radiative fluxes were reported in ECMWF by  
125 applying the prognostic aerosols compared to the monthly climatological aerosol  
126 (Rémy et al., 2015). Toll et al. (2016) found that the inclusion of aerosol effects in  
127 NWP system was beneficial to the accuracy of simulated radiative fluxes, temperature  
128 and humidity in the lower troposphere over Europe. In addition, it was shown that the  
129 quality of weather forecasts at UK MET office can be further advanced when the  
130 real-time aerosol distribution rather than climatological distribution was included,

131 with the decreased bias of downward SW at surface ( $-2.79 \text{ W m}^{-2}$  vs.  $-5.30 \text{ W m}^{-2}$ )  
132 and the mean sea-level pressure (0.71hPa vs. 0.80hPa) (Mulcahy et al., 2014; Toll et  
133 al., 2015). For these research serving for operational NWP systems, both online and  
134 offline approaches (that aerosol information were simulated by separate chemistry  
135 system and then offline coupled to NWP model) were widely used.

136 In most previous research-targeted modeling studies over northern China, the  
137 aerosol-radiation interaction has been widely assessed in online-coupled  
138 meteorology-chemistry models, which might not be practical for NWP purpose.  
139 Considering aerosol particles differ by morphology, size and chemical composition,  
140 therefore, the numerical treatment of aerosol particles in atmospheric models needs  
141 sophisticated method and considerable simplifications, which may bring in more  
142 assumptions and uncertainties in online coupling (Baklanov et al., 2014). Moreover,  
143 the online simulations require quite high computational costs and could not meet the  
144 requirement of efficiency for operational NWP. Grell and Baklanov (2011) illustrated  
145 that the offline approach could generate to almost identical results compared to online  
146 simulation with the offline-coupling intervals about 0.5-1h. Thus, the  
147 computational-economic offline simulation provides a feasible and computationally  
148 less demanding approach to include the aerosol-radiation interaction in an operational  
149 NWP system. Péré et al. (2011) adopted an offline-coupling between the  
150 chemistry-transport model CHIMERE and WRF to study the radiative forcing of high  
151 load aerosols during the heat wave of summer in 2003 over Western Europe. Wang et



152 al. (2018) offline implemented the daily AOD from Moderate Resolution Imaging  
153 Spectroradiometer (MODIS) to WRF during a heavy winter pollution at Beijing to  
154 study the effect of aerosols on boundary layer. Still, there have been few studies that  
155 adopted offline simulation to investigate the impacts of aerosol-radiation interactions  
156 over northern China in an NWP system. At Institute of Urban Meteorology, regional  
157 operational NWP system–RMAPS-ST (adapted from WRF) and regional air quality  
158 model–RMPSA-Chem (adapted from WRF-Chem) were applied operationally. In this  
159 study, we investigate the radiative effects of aerosols and their feedbacks on weather  
160 forecasting over northern China during a polluted event occurred in winter of 2015,  
161 and further potential impacts of changed meteorology to the transport and dissipation  
162 of pollution. The simulations were in the configurations of the two systems, aiming at  
163 presenting the offline-coupling of the high-frequent real-time aerosol distribution  
164 simulated by WRF-Chem and WRF, and evaluating the potential effects of  
165 aerosol-radiation interactions on the forecast skills in the RMAPS-ST system for  
166 future applications.

167 The remainder of the paper is organized as follows. Section 2 presents the model  
168 configuration and experimental design. In section 3, the model’s capabilities in  
169 capturing and forecasting the pollution episode are validated with observations first,  
170 and impacts of aerosol-radiation interactions on meteorological forecasting over  
171 northern China are analyzed further. The final section provides the concluding  
172 remarks.

## 173 **2. Model description and experimental design**

174 WRF is a state-of-the-art atmospheric modeling system designed for both  
175 meteorological research and NWP. The WRF version 3.8.1 released in August, 2016  
176 was used in this study for a domain covering the northern China with a horizontal  
177 resolution of 9km ( $222 \times 201$  grid points, Fig. 1a), and for 50 vertical levels. The  
178 lateral boundary conditions (BCs) and initial conditions (ICs) for meteorological  
179 variables are provided by the forecast of ECMWF. The major physical schemes  
180 include the Assymetric Convective Model Version 2 (ACM2) PBL scheme (Pleim,  
181 2007), the Thompson microphysics without aerosol-aware option (Thompson et al.,  
182 2008), the Kain-Fritsch cumulus parameterization (Kain, 2004), and the National  
183 Center for Environmental Prediction, Oregon State University, Air Force, and  
184 Hydrologic Research Lab's (NOAH) land-surface module (Chen and Dudhia, 2001;  
185 Ek et al., 2003). The landuse data have been reprocessed, with a higher accuracy and  
186 finer classification for urban areas (Zhang et al., 2013) and the urban canopy model  
187 (UCM) was not activated.

188 The shortwave and longwave radiation scheme is the Rapid Radiative Transfer  
189 Model for General Circulation Models (RRTMG) (Iacono et al., 2008). The RRTMG  
190 scheme is a new version of RRTM added in Version 3.1, and includes the Monte  
191 Carlo Independent Column Approximation (MCICA) method of random cloud  
192 overlap. A recent intercomparison study showed that the RRTMG had relatively  
193 smaller mean errors in solar flux at the surface and the top of the atmosphere

194 (Oreopoulos et al., 2012) and was considered as recommended WRF configuration  
195 for air quality modeling (Rogers et al., 2013). The RRTMG scheme is capable to  
196 include the climatological aerosol data with spatial and temporal variations or an  
197 external time varying 3D aerosol input through the option of AER\_OPT (Ruiz-Arias  
198 et al., 2014). In the present study, the real-time hourly aerosol optical depth (AOD)  
199 at 550nm from external files was input into WRF following the second approach.  
200 The AOD at 550nm was calculated as the vertical integral of extinction coefficients at  
201 550nm from WRF-Chem simulation.

202 WRF-Chem version 3.3.1 was applied in this study, and the horizontal  
203 resolution was 9 km, with 222×201 grid points covering northern China, which was  
204 the same configuration of WRF mentioned above. WRF-Chem simulates the formation,  
205 transformation and transport processes of both primary and secondary atmospheric  
206 pollutants, including gases and PM species (Zhao et al., 2019). Physical  
207 parameterizations included single-layer Urban Canopy Model, Noah land-surface,  
208 Yonsei University (YSU) PBL, Grell-Devenyi ensemble convection, Thompson  
209 microphysics, and RRTM longwave and Goddard shortwave radiation (Chen and  
210 Dudhia, 2001; Hong et al., 2006; Grell and Dévényi, 2002; Thompson et al., 2008;  
211 Mlawer et al., 1997; Chou and Suarez, 1999). Carbon bond mechanism Z (CBMZ)  
212 including comprehensive reactions and alterable scenarios were used as the  
213 gas-phase mechanism. Model for Simulating Aerosol Interactions and Chemistry  
214 (MOSAIC) are used with four size bins (Zaveri and Peters, 1999). Anthropogenic

215 emission data were from the MEIC (2012) inventory (<http://www.meicmodel.org/>)  
216 with a resolution of  $0.1^\circ \times 0.1^\circ$ . Meteorological ICs and BCs were obtained from the  
217 Final Analysis data (FNL) with a resolution of  $1.0^\circ \times 1.0^\circ$  from the National Centers  
218 for Environmental Prediction (NCEP). To generate aerosol fields for study period  
219 (Dec. 2<sup>nd</sup>-11<sup>th</sup>), 9-days WRF-Chem simulations from Dec. 2<sup>nd</sup> were conducted using  
220 prescribed idealized profiles as ICs and BCs for chemical species.

221 To estimate the aerosol radiative forcing and its feedbacks on meteorological  
222 fields, two sets of 24-hour WRF forecasts were conducted at 00UTC from 2<sup>nd</sup>-10<sup>th</sup>  
223 December 2015. The only difference between the two sets of forecasts is whether the  
224 aerosol radiative feedback is activated (Aero, with WRF-Chem simulated hourly  
225 AOD fields as input fields) or not (NoAero, no aerosol included), and other schemes  
226 remained the same. It is noted that the aerosol-cloud interactions were not included  
227 in the study.

228 The sites of observations over simulated domain and northern China plain (NCP,  
229 purple box in Fig. 1a) were shown in Fig. 1. The 550nm AOD retrievals from Level  
230 2 of MODIS sensors onboard polar orbiting satellites Terra and Aqua satellites were  
231 adopted to evaluate the spatial distribution of modeled AOD. The vertical  
232 distribution of aerosol extinction coefficient at 550nm were compared with that from  
233 Cloud-Aerosol Lidar and Infrared Pathfinder Satellite Observations (CALIPSO)  
234 satellite. Moreover, three sites of AEROSOL ROBOTIC NETWORK (AERONET) were  
235 used to validate the simulation (black dots in Fig. 1b), and the observed AOD

236 obtained from observation at the Institute of Atmospheric Physics (IAP), Chinese  
237 Academy of Sciences (39°58' 28" N, 116°22' 16" E) in Beijing city (blue dot in  
238 Fig. 1b) was also included as supplementary. The hourly observed PM<sub>2.5</sub>  
239 concentrations of total 813/332 monitoring stations over the study domain/NCP  
240 were from the released data by the China National Environmental Monitoring Centre  
241 (<http://106.37.208.233:20035/>, colored dots in Fig. 3a). For given cities (dots in Fig.  
242 1a), hourly PM<sub>2.5</sub> concentration was represented by the average of data from all  
243 monitoring sites located in the city. Simulated meteorological variables including  
244 2-m temperature and wind speed at 10m were evaluated using in-situ observations  
245 from National Meteorological Information Center  
246 (<http://data.cma.cn/data/cdcindex.html>) of China Meteorological Administration  
247 (CMA, dots in Fig. 8a). The radiations were observed at IAP and in-situ stations of  
248 CMA (shown as triangles in Fig. 1a). The vertical observation of atmospheric wind  
249 speed from sounding were also used (circles in Fig. 1a). The variables, sources,  
250 numbers of sites in the domain and NCP and the frequency of chemical and  
251 meteorological observations were also listed in Table 1.

### 252 **3. Results**

#### 253 **3.1 Evaluation of AOD and PM<sub>2.5</sub> simulated by WRF-Chem**

254 Before the offline-coupling of the WRF-Chem simulated hourly AOD to  
255 meteorological model WRF, we first validated the simulated AOD and ensured the  
256 model's capability to reproduce the features of the aerosol field. Figure 2 shows the

257 spatial distribution of modeled AOD and AOD from MODIS Terra and Aqua. It was  
258 seen that WRF-Chem is capable to capture the AOD spatial distribution and also  
259 reproduced the transport paths during the event. The simulated high-valued AOD  
260 located in Henan on Dec. 6<sup>th</sup>, then the center moved to Hebei and Beijing on 7<sup>th</sup> and  
261 shifted to northeast areas afterwards. The variations of simulated AOD were in  
262 consistent with both Terra and Aqua with slightly overestimated peak value of AOD.  
263 In particular, the simulated shifting of AOD center to northeast areas was also  
264 observed in Aqua (Fig. 2r-s). To further verify the vertical distribution of aerosol  
265 extinction coefficient, Fig. 3 displayed the vertical distribution of simulated 550nm  
266 aerosol extinction coefficient compared to those from CALIPSO. Four cross sections  
267 along CALIPSO paths on 6<sup>th</sup> to 9<sup>th</sup> December were shown. The results indicated that  
268 the model could generally reproduce the vertical distribution of extinction  
269 coefficients at 550nm in terms of comparable magnitude with those from CALIPSO,  
270 particularly on 6<sup>th</sup>, 7<sup>th</sup> and 9<sup>th</sup>, December. However, CALIPSO showed more high  
271 values at lower altitude (below 1km) that model failed to capture; the inconsistency  
272 may be associated with both CALIPSO retrieval uncertainties at the low altitude and  
273 the model itself. Figure 4 further displayed the temporal variation of simulated AOD  
274 at 550nm (blue solid) at four sites, in comparison with three AERONET stations  
275 (black circles in Figs. 4a-c) and IAP site (black circles in Fig. 4d) for the period  
276 during 3<sup>rd</sup> to 11<sup>th</sup> December, 2015 (local time, LT). As shown in blue solids in Fig.  
277 4a, the simulated AOD increased since 6<sup>th</sup> Dec. and reached the peak value of 9 on

278 7<sup>th</sup>, and the high AOD value maintained until 9<sup>th</sup> and reached the second peak. The  
279 second peak was also observed from AERONET though most of them were missing  
280 during the pollution event. The temporal variations of AOD at Beijing-CMA and  
281 IAP (Figs. 4b and d) were similar to those at Beijing station (Fig. 4a). Meanwhile,  
282 the simulated AOD at Xianghe (Fig. 4c) was relatively lower than those at other  
283 stations.

284 Considering that the aerosol extinction was mainly attributed to scattering and  
285 absorption of solar radiation by PM<sub>2.5</sub> and their hygroscopic growth with relative  
286 humidity (Cheng et al., 2006), next we compared the simulated PM<sub>2.5</sub> concentrations  
287 with corresponding in-situ observation over the model domain. As shown in Fig. 5,  
288 the simulated and observed pollution were both initiated over Henan province on 6<sup>th</sup>,  
289 further intensified and shifted northward afterwards. The polluted center located  
290 over south of Hebei province and maintained until 10<sup>th</sup>, with the maximum PM<sub>2.5</sub>  
291 concentration exceeding 440 $\mu\text{g m}^{-3}$ . The results indicated that WRF-Chem could  
292 well capture the spatial features of PM<sub>2.5</sub> and its temporal variation, in spite of the  
293 slight discrepancy of the center position during 9<sup>th</sup> and 10<sup>th</sup>. Figure 6 displayed the  
294 mean bias, root mean square error (RMSE), and correlation coefficient during the  
295 heavy pollution and relatively cleaner periods. It was seen that the biases of PM<sub>2.5</sub>  
296 were generally less than 40  $\mu\text{g m}^{-3}$  with the correlation coefficient exceeding 0.8  
297 during clean period (Fig. 6a-c). Compared with clean period, the bias and RMSE  
298 were generally larger during polluted period (Fig. 6d-f). The PM<sub>2.5</sub> concentrations

299 over most areas of the domain were underestimated with the maximum bias  
300 exceeding  $160\mu\text{g m}^{-3}$ . Overall, the correlation coefficient was generally higher than  
301 0.4 in northern China during the polluted period, particularly over Beijing with the  
302 correlation coefficient reaching 0.8.

303 To further assess the temporal evolutions of the pollution, the simulated  $\text{PM}_{2.5}$   
304 concentrations at three major cities (Beijing, Shijiazhuang and Tianjin, shown as  
305 black dots in Fig. 1a) and two provinces (Hebei and Henan) in northern China were  
306 compared with observation as shown in Fig. 7. It showed that the hourly variations  
307 of  $\text{PM}_{2.5}$  concentration, including the occurrence of several high peaks at the three  
308 cities, as well as the gradual accumulation of pollution in Hebei and Henan could be  
309 reasonably reproduced by WRF-Chem. The correlation coefficients (R) between  
310 simulation and observation at Beijing, Shijiazhuang, Tianjin, Hebei and Henan were  
311 0.85, 0.89, 0.76, 0.92 and 0.77 respectively. It should be noted that there exists slight  
312 overestimation (underestimation) of the peak magnitude during 9<sup>th</sup> to 10<sup>th</sup> at Beijing  
313 and Shijiazhuang (Tianjin, Hebei and Henan); the overestimation in Beijing and  
314 Shijiazhuang is possibly associated with the frequent emission changes caused by  
315 emission-control-measures in reality which are not dynamically updated in the model;  
316 the underestimation is more related with the deficiency of model skills, such as  
317 missing heterogeneous reaction paths in the chemistry scheme.

### 318 **3.2 Aerosol effects on meteorological simulations**

319 In this section, the influences of aerosol-radiation interaction on the spatial and



320 temporal variations of radiation and energy budget simulated by WRF model were  
321 analyzed, and their impacts on the forecasts of meteorological fields were discussed  
322 further.

### 323 **3.2.1 Aerosol impacts on simulations of radiative forcing and heat fluxes**

324 To illustrate the impacts of aerosol-radiation interaction on the forecasts of  
325 radiation during the pollution event, the simulated surface downward SW radiation  
326 and net radiation at Beijing, Tianjin, Taiyuan and Jinan, as denoted by the triangles  
327 in Fig. 1a, were compared with observations in Fig. 8. To show the relationship with  
328 aerosol, the time series of AOD for Dec. 3<sup>th</sup> -11<sup>th</sup> were overlaid as gray shadings in  
329 Fig. 8. During the clean stage with quite low AOD values (close to 0) before 6<sup>th</sup> Dec.,  
330 both simulations with and without aerosols reasonably reproduced the temporal  
331 variation of downward SW at Beijing despite the slightly overestimation during the  
332 noon-time (Fig. 8a). However, the overestimated downward SW in NoAero turned  
333 to intensify extensively since 6<sup>th</sup> Dec. and sustained till 10<sup>th</sup> Dec., accompanied by  
334 the occurrence of the pollution with the high AOD value. Meanwhile, the downward  
335 SW was much lower in Aero than that in NoAero due to aerosol extinction, with  
336 resembled temporal variations and comparable magnitude at the peak time compared  
337 to the observations. Similarly, the variations of downward SW from Aero simulation  
338 were also closer to observations at Tianjin, Taiyuan and Jinan than those in NoAero  
339 (Figs. 8b-d). It was noted that the most significant improvement of simulated  
340 downward SW at Jinan appeared on 10<sup>th</sup> Dec. and was later than that at Beijing,

341 which was consistent with the AOD's variations at Jinan. Moreover, the surface  
342 energy balance was also affected by the reduction of downward SW radiation  
343 reaching the ground due to the presence of aerosol particles. As shown in Figs. 8e–h,  
344 in corresponding to the changes in downward SW, the variations of net radiation at  
345 surface in Aero were also in better agreement with observation during the polluted  
346 period than in NoAero, particularly during daytime with the high AOD values.

347 To further quantify the influence of the aerosol-radiation interaction on the  
348 diurnal variation of surface radiation, next we compared the simulated averaged  
349 diurnal variation of downward SW and net radiation during the polluted episode (6<sup>th</sup>  
350 to 10<sup>th</sup>) with observation. Figure 9a showed that there existed a large overestimation  
351 of surface downward SW during the daytime in NoAero. Particularly, the  
352 overestimated downward SW tended to increase since morning (0800 LT) and peak  
353 at noon (1300 LT) with the maximum bias reaching  $226.5 \text{ W m}^{-2}$ , and the mean bias  
354 of  $\sim 149.4 \text{ W m}^{-2}$  during daytime (averaged during 0800 to 1800 LT, Table 2).  
355 However, the overestimated SW radiation was remarkably reduced in Aero with the  
356 mean bias of  $38.0 \text{ W m}^{-2}$  during daytime. Similarly, the diurnal variation and  
357 magnitude of downward SW radiation at surface were also better captured at Tianjin,  
358 Taiyuan and Jinan in Aero (Figs. 9b–d), with the lower bias ( $70.9 \text{ W m}^{-2}$ ,  $118.3 \text{ W}$   
359  $\text{m}^{-2}$  and  $97.7 \text{ W m}^{-2}$ ) than in NoAero ( $115.5 \text{ W m}^{-2}$ ,  $155.0 \text{ W m}^{-2}$  and  $149.1 \text{ W m}^{-2}$ )  
360 during daytime. Note the biases of SW radiation in Tianjin, Taiyuan and Jinan were  
361 not improved as much as in Beijing due to the lower AOD. Consistent with this

362 finding, the reduction of downward SW was also reported in United States (Zhang et  
363 al., 2010) and Europe (Toll et al., 2016) with relatively lower decrease ( $10 \text{ W m}^{-2}$   
364 and  $18 \text{ W m}^{-2}$ ); the relatively larger reductions ( $30\text{-}110 \text{ W m}^{-2}$ ) in northern China is  
365 possibly due to the higher aerosol load. Figures 9e–h presented the diurnal variations  
366 of net radiation, with positive (negative) net radiation during daytime (nighttime) in  
367 observation, and the NoAero tended to overestimate (underestimate) the net  
368 radiation at surface during daytime (nighttime), indicating that there existed surplus  
369 energy income and outcome in model than those in observation, inducing the larger  
370 magnitude of diurnal cycle of net radiation. By including the aerosol-radiation  
371 interaction in the model, the simulated diurnal variations of net radiation were  
372 markedly improved, particularly during daytime with the reduction of bias by 85.3%,  
373 50.0%, 35.4%, and 44.1% at Beijing, Tianjin, Taiyuan and Jinan, respectively.

374 In response to the decrease of downward SW radiation and net radiation at the  
375 ground during daytime, the surface fluxes also changed in presence of aerosol  
376 extinction within the energy-balanced system. Figure 10 displayed the difference of  
377 surface sensible and latent heat flux between Aero and NoAero at 1300LT, when the  
378 influences of the aerosol on radiation reaching the peak. Comparing to the NoAero  
379 simulation, both the surface sensible and latent heat flux emitted by the surface were  
380 reduced in the Aero simulation, with the domain-average of  $16.1 \text{ W m}^{-2}$  (18.5%) and  
381  $6.8 \text{ W m}^{-2}$  (13.4%) respectively. It was noted that the decrease of the surface latent  
382 heat flux was less pronounced than that of surface sensible heat flux, suggesting the

383 impact of aerosol-radiation interaction on the humidity was less significant than that  
384 of temperature, which was also reported over United States (Fan et al., 2008) and  
385 western Europe (Péré et al., 2011).

### 386 **3.2.2 Aerosol impacts on simulations of temperature, PBLH and wind fields**

387 The changes in radiation and energy budget through the impacts of  
388 aerosol-radiation interaction would certainly induce the changes in PBL  
389 thermodynamics and dynamics, which would result in changes in the forecasts of  
390 meteorological fields. The impacts on the forecasts of 2-m temperature, PBLH and  
391 wind fields due to the aerosol-radiation interaction are discussed in the following  
392 subsection.

393 Figure 11 presented the diurnal variation of averaged bias of 2-m temperature  
394 during polluted period in NoAero (upper panel) and Aero (lower panel) compared  
395 with the in-situ observation during 1100 LT to 2300 LT. It was obvious that the  
396 temperature of NoAero was significantly overestimated for a wide range over  
397 northern China, particularly over the plain areas including south of Hebei, Henan  
398 and Shanxi provinces. The warm biases tended to intensify in the afternoon and  
399 reach  $\sim 3^{\circ}\text{C}$  over south part of Hebei province (Figs. 11b–c). Accompanied by the  
400 warm biased over plain areas throughout the day, the mountain areas were  
401 dominated by the cold biases until 1700 LT, and turned to be warm biases afterwards,  
402 which were attributed by the frozen water in soil due to wet bias of soil moisture  
403 over mountain areas, inducing overestimated energy transport from atmosphere to

404 soil during daytime. Compared to NoAero, the lower temperature in Aero due to the  
405 decreased surface solar radiation, caused by aerosol extinction led to the reduced  
406 warm bias in NCP region. However, the cold bias in Beijing area was slightly  
407 intensified, which may partly relevant with the overestimated PM<sub>2.5</sub> concentration in  
408 Beijing and can be improved by incorporating more accurate aerosol information in  
409 the future. It was noted that the cold biases over mountain areas associated with the  
410 model physics deficiency can not be corrected by aerosol-radiation effects, thus the  
411 correction of aerosol-radiation effect may get complex results and differ with  
412 regions due to the model pre-existing deficiencies.

413 To quantitatively evaluate the agreement of simulated 2-m temperature with  
414 observations, the mean bias and RMSE were employed, and their averaged diurnal  
415 variations during the polluted episode (6<sup>th</sup> to 10<sup>th</sup>, Dec.) averaged over NCP, denoted  
416 by the purple box in Fig. 1a, were displayed in Fig. 12. As shown in Fig. 12a, the  
417 warm bias in NoAero sustained during the entire 24-hr forecast, ranging from 0.3 °C  
418 to 0.9 °C. Compared to NoAero, the NCP area-averaged warm bias was remarkably  
419 reduced by ~0.40°C (~73.9%) due to aerosol-radiation interaction, with the  
420 maximum reaching ~0.54 °C (~95.0 %) at 1100 LT (Figs. 12a and c). Consistently  
421 with mean bias, the RMSE was also lower in Aero than NoAero, particularly during  
422 1100 to 2000 LT during the daytime (Figs. 12b and d).

423 The aerosol-radiation interaction may also have profound impacts on atmospheric  
424 structure in addition to radiation and temperature (Rémy et al., 2015). PBLH is one

425 of the key parameters to describe the structure of PBL and closely related to air  
426 pollution. It was indicated that the mean daytime PBLH over northern China were  
427 around 300–600m (Fig. 13a), and declined generally 40–200m (10%–40%) in Aero  
428 over the region with highest PM<sub>2.5</sub> concentration, particularly over Beijing, Tianjin  
429 and Hebei (Figs. 13b–c). As shown in dashed lines in Fig. 14, the NCP  
430 area-averaged PBLH at noon-time (1400 LT) was diminished dramatically by  
431 aerosol-radiation interaction during the pollution event over northern China, with the  
432 maximum decrease reaching -155.2m on 7<sup>th</sup> Dec. The reduction of PBLH could be  
433 the consequence of more stable atmosphere in Aero than NoAero, which was  
434 induced by the terrestrial cooling in the lower part of the planetary boundary layer  
435 and the solar heat due to the absorbing in the upper layers (solid lines in Fig. 14).

436 The near surface wind fields changes due to aerosol-radiation interaction were  
437 further investigated. Figure 15 shows the wind vector in NoAero (upper panel), Aero  
438 (middle panel) and their difference (lower panel). It can be seen from Fig. 15a-e that  
439 the northern China was dominated by the anticyclonic circulation, accompanied by  
440 the relatively weaker northeast wind over Beijing and Hebei areas. The comparisons  
441 of Aero and NoAero (Figs. 15 k-o) showed that the northeast wind was increased  
442 with the maximum reaching 1 m s<sup>-1</sup> by aerosol-radiation interaction over Beijing  
443 and Hebei, where high particles concentration located (shadings in Figs. 15 f-j).  
444 Figures 15k-o also indicated the changes of west wind over the south part of the  
445 domain and southeast wind over the ocean areas, which tended to weaken the

446 anticyclonic circulation and thus declined the wind speed there. The reduced wind  
447 speed due the inclusion of aerosol-radiation interaction was possible due to the  
448 thermal-wind adjustment in response to the more stable near-surface atmosphere,  
449 which was also addressed in previous work using WRF-Chem (Zhang et al., 2015).

450 The comparisons between simulated wind speeds against in-situ observation  
451 averaged during 6<sup>th</sup> to 10<sup>th</sup> Dec. were displayed in Fig. 16. In regard of NoAero, the  
452 simulated wind speed at 10m was overestimated over the nearly whole domain with  
453 the maximum bias up to  $3 \text{ m s}^{-1}$  except some mountain sites (upper and middle  
454 panels in Fig.16). It might be due to the omission of UCM model as the  
455 overestimation is more prominent in city clusters (especially in Beijing and southern  
456 Hebei) than other areas. Figures 16k-o showed the difference of absolute value of  
457 bias between Aero and NoAero and indicated the bias of simulated wind speed were  
458 decreased over south and northeast part of the domain during afternoon (Figs. 16k-m)  
459 by aerosol-radiation interaction, while were increased over Beijing and Hebei area  
460 particularly during nightfall (Fig. 16n) due to the intensified wind speed there. The  
461 NCP area-averaged bias and RMSE of wind speed at 10m were further shown in  
462 Figure 17. It was seen that the aerosol-radiation interaction helped to reduce the  
463 overestimation of wind speed at 10m up to  $0.08 \text{ m s}^{-1}$  ( $\sim 7.8\%$ ), particular during  
464 daytime (Figs. 17a and c). Correspondingly, the RMSE of Aero was also lower than  
465 that of NoAero, indicating that the inclusion of aerosol-radiation interaction helped  
466 to improve the prediction of near surface wind speed on the domain-averaged scale.

467 Although the changes of wind speed are less straightforward than that of radiation,  
468 the aerosol-radiation interactions can also affect dynamic fields (vertical wind shear)  
469 through the changes of atmospheric thermal structure and the thermal wind relation  
470 when the interaction lasts long enough (Huang et al., 2019). Figure 18 displayed  
471 vertical profiles of wind speed at the stations of Beijing and Xingtai in simulation  
472 and verified with sounding observations. It was shown that the NoAero  
473 underestimated (overestimated) the low levels wind speed at 0800 LT (2000 LT) at  
474 both Beijing and Xingtai. However, the wind speed was increased (decreased) at  
475 0800 LT (2000 LT) in Aero relative to NoAero, indicating the positive impacts on  
476 the simulation of atmospheric winds by aerosol-radiation interaction.

477 Since the forecast meteorological fields by WRF (RMPAS-ST) is routinely  
478 applied to WRF-Chem (RMAPS-Chem) as meteorological ICs in the air quality  
479 operational system at IUM, the changed meteorology due to aerosol-radiation  
480 interaction will further influence the forecast of pollution through meteorological  
481 ICs. In regard of further feedback of aerosol-radiation interactions to the transport  
482 and dissipation of the pollutants, their impacts on wind field at 850hPa were further  
483 discussed as it is strongly correlated with haze formation (Zhang et al., 2018; Zhai et  
484 al., 2019). Figures 19 a-e display that northern China was dominated by the  
485 anticyclone circulation at 850hPa, associated with the southwest (northwest) wind in  
486 the west (east) of the northern part of the domain. The difference of U (zonal,  
487 eastward is positive) winds between Aero and NoAero (middle panel in Fig. 16)



488 showed that the U wind was intensified over west Hebei, accompanied by the quite  
489 small changes in Beijing area, indicating that the increased U wind was blocked by  
490 the mountains and could not transport the pollutants over Hebei and Beijing to the  
491 east (Figs. 19 f-h). On the other hand, the changes of V (meridional, northward is  
492 positive) show different patterns over north and south of the  $38^{\circ}$  N (lower panel in  
493 Fig. 19). In the south part, the increased northward wind due to aerosol-radiation  
494 interaction may help to transport pollutants from highly polluted areas to Hebei and  
495 Beijing. In the north of the domain, the negative (positive) changes of V wind  
496 indicated the reduced northward (southward) wind in west (east) of Hebei, which  
497 could suppress the diffusion of the pollutants. As a result, both U and V changes  
498 induced by the aerosol-radiation interaction will prevent pollutants from dispersing  
499 and may exacerbate the pollution in Heibeii and Beijing, which confirms the more  
500 stable boundary layer due to aerosol-radiation interaction as discussed earlier.

#### 501 **4. Concluding remarks**

502 To facilitate the future inclusion of aerosol-radiation interactions in the regional  
503 operational NWP system – RMAPS-ST (adapted from WRF) at IUM, CMA, the  
504 impacts of aerosol-radiation interactions on the forecast of surface radiation and  
505 meteorological parameters during a heavy pollution event (Dec. 6<sup>th</sup> -10<sup>th</sup>, 2015) over  
506 northern China were investigated. The aerosol information (550-nm AOD 2D field)  
507 were simulated by WRF-Chem and then offline-coupled into RRTMG radiation  
508 scheme of WRF to enable the aerosol-radiation feedback in the forecast. Two sets of

509 24-hour forecasts were performed at 00UTC from Dec. 2<sup>nd</sup>-11<sup>th</sup>, 2015. The only  
510 difference between the two sets of forecasts was whether the aerosol radiative  
511 feedback was activated (Aero, with WRF-Chem simulated hourly AOD fields as  
512 input fields) or not (NoAero, no aerosol included), while the other schemes  
513 remained the same.

514 The capability of WRF-chem to reproduce the polluted episode was confirmed  
515 first before the offline-coupling of AOD to WRF. The validation of simulated AOD  
516 and aerosol extinction coefficient against MODIS and CALIPSO confirmed that the  
517 model could reproduce both the spatial and vertical distribution of 550nm AOD.  
518 Further results indicated that the temporal variations of simulated AOD at 550nm  
519 was in consistent with AERONET and in-situ observation at IAP. In addition, the  
520 spatial distributions of PM<sub>2.5</sub> as well as their magnitude, particularly during the peak  
521 stage (8<sup>th</sup> to 9<sup>th</sup>) of the pollution event were reasonably captured by WRF-Chem,  
522 with the correlation coefficients of 0.85, 0.89, 0.76, 0.92 and 0.77 at Beijing,  
523 Shijiazhuang, Tianjin, Hebei and Henan, respectively.

524 Further, the impacts of aerosols-radiation interaction on the forecasts of surface  
525 radiation, energy budget, and meteorology parameters were evaluated against  
526 surface and sounding observations. The results showed that the decrease of  
527 downward SW radiation reaching surface induced by aerosol effects helped to  
528 reduce the overestimation of SW radiation during daytime. Moreover, the simulated  
529 surface radiation budget has also been improved, with the biases of net radiation at

530 surface decreased by 85.3%, 50.0%, 35.4%, and 44.1% during daytime at Beijing,  
531 Tianjin, Taiyuan and Jinan respectively, accompanied by the reduction of sensible  
532 ( $16.1 \text{ W m}^{-2}$ , 18.5%) and latent ( $6.8 \text{ W m}^{-2}$ , 13.4%) heat fluxes emitted by the  
533 surface at noon-time.

534 The energy budget changed by aerosol extinction further cools 2-m temperature  
535 by  $\sim 0.40^\circ\text{C}$  over NCP, reducing warm bias by  $\sim 73.9\%$  and also leading to lower  
536 RMSE, particularly during daytime. Since aerosol cools the lower planetary  
537 boundary layer and meanwhile warms the high atmosphere, it induced the more  
538 stable stratification of the atmosphere and the declination of PBLH by 40–200m  
539 (10%–40%) over NCP. Associating with the changes of planetary boundary structure  
540 and more stable near-surface atmosphere, the aerosol-radiation interaction tended to  
541 weaken the anticyclonic circulation including the east wind over the south part of  
542 the domain and northwest wind over the ocean areas. Thus the bias of wind speed  
543 over south and northeast part of the domain were decreased particularly during the  
544 afternoon, while increased over Beijing and Hebei area. In regard of NCP-average,  
545 the overestimated 10m wind speed was improved during whole day with the  
546 maximum up to  $0.08 \text{ m s}^{-1}$  ( $\sim 7.8\%$ ) at 1400LT. The comparison between simulated  
547 vertical profiles of atmospheric wind speed with soundings also indicated that Aero  
548 was in better agreement with observation and aerosol-radiation interaction helped to  
549 improve the prediction of dynamic fields such as atmospheric wind through the  
550 thermal wind relation by altering the atmospheric structure.

551 The impacts of aerosol-radiation interactions on wind field at 850hPa were  
552 further discussed. The results showed that aerosol-radiation interaction will prevent  
553 pollutants from dispersing and may exacerbate the pollution through changes of both  
554 U and V wind, which confirms the more stable boundary layer due to  
555 aerosol-radiation. These wind field changes may also influence the forecast of the  
556 transport and dissipation of the pollutants by WRF-Chem through changed  
557 meteorological ICs.

558 This study analyzed the impacts of aerosol-radiation interaction on radiation and  
559 meteorological forecast by using the offline-coupling of WRF and high-frequent  
560 updated AOD simulated by WRF-Chem, which is more computationally economic  
561 than the online simulation with the integration time for 96h forecast of about 40% of  
562 that for online simulation. This approach allows for a potential application to include  
563 aerosol-radiation interaction in our current operational NWP systems. The results  
564 revealed that aerosol-radiation interaction had profound influence on the  
565 improvement of predictive accuracy and the potential prospects for its application in  
566 regional NWP in northern China. To verify the statistically significance of the  
567 results, we further conducted the 24-hour forecasts for a longer period lasting 27  
568 days (Jan. 13<sup>th</sup> – Feb. 8<sup>th</sup>, 2017), with no AOD field (NoAero) and WRF-Chem  
569 simulated hourly AOD fields (Aero) included, as well as constant AOD value of  
570 0.12 (ClimAero), respectively. The results showed that the mean RMSE of 2-m  
571 temperature (wind speed at 10m) in Aero and ClimAero relative to NoAero was

572 reduced by 4.0% (1.9%) and 1.2% (1.6%), respectively (not shown). The one-month  
573 results indicated that the simulation with the inclusion of WRF-Chem simulated  
574 hourly AOD fields outperformed other two simulations and showed more  
575 improvement on the meteorological forecast than the simulation with climatological  
576 AOD fields. More detailed evaluations and analysis will be addressed in a future  
577 article. As the simulated AOD was adopted in the present study, it should be noted  
578 that there exists a discrepancy between simulated AOD and observation in both  
579 spatial distribution and temporal variation, which may influence the impacts of  
580 aerosol-radiation interaction. Meanwhile, surface energy budget and atmospheric  
581 dynamics are also influenced by aerosol-cloud interaction, which are related to cloud  
582 microphysical processes and are not discussed in this study.

583 **Data availability** Data are available upon request from the first authors Yang Yang  
584 (yyang@ium.cn) and corresponding authors Xiujuan Zhao (xjzhao@ium.cn) and Dan  
585 Chen (dchen@ium.cn).

586

587 **Author contribution** Yang Yang, Min Chen, Xiujuan Zhao and Dan Chen designed the  
588 experiments, Yang Yang and Xiujuan Zhao performed the simulations and carried them  
589 out. Yang Yang and Dan Chen prepared the manuscript with contributions from all  
590 co-authors.

591

592 ***Competing interests*** The authors declare that they have no conflict of interest.

593

594 ***Acknowledgments*** This work was jointly supported by the National Key R&D  
595 Program of China (grant nos. 2017YFC1501406 and 2018YFF0300102), Natural  
596 Science Foundation of Beijing Municipality (8161004), the National Natural Science  
597 Foundation of China (grant nos. 41705076, 41705087 and 41705135),  
598 Beijing Major Science and Technology Project (Z181100005418014) and Beijing  
599 Natural Science Foundation (grant no. 8204074).

600

601 **Reference**

- 602 Ackerman, A. S., Toon, O. B., Stevens, D. E., Heymsfield, A. J., Ramanathan, V.,  
603 and Welton, E. J.: Reduction of tropical cloudiness by soot, *Science*, 288, 1042–  
604 1047, <https://doi.org/10.1126/science.288.5468.1042>, 2000.
- 605 Baklanov, A., Schlünzen, K., Suppan, P., Baldasano, J., Brunner, D., Aksoyoglu, S.,  
606 Carmichael, G., Douros, J., Flemming, J., Forkel, R., Galmarini, S., Gauss, M.,  
607 Grell, G., Hirtl, M., Joffre, S., Jorba, O., Kaas, E., Kaasik, M., Kallos, G., Kong,  
608 X., Korsholm, U., Kurganskiy, A., Kushta, J., Lohmann, U., Mahura, A.,  
609 Manders-Groot, A., Maurizi, A., Moussiopoulos, N., Rao, S. T., Savage, N.,  
610 Seigneur, C., Sokhi, R. S., Solazzo, E., Solomos, S., Sørensen, B., Tsegas, G.,  
611 Vignati, E., Vogel, B., and Zhang, Y.: Online coupled regional meteorology  
612 chemistry models in Europe: current status and prospects, *Atmos. Chem. Phys.*,  
613 14, 317–398, <https://doi.org/10.5194/acp-14-317-2014>, 2014.
- 614 Chan, C. K. and Yao, X.: Air pollution in mega cities in China, *Atmos. Environ.*, 42,  
615 1–42, <https://doi.org/10.1016/j.atmosenv.2007.09.003>, 2008.
- 616 Chen, D., Liu, Z., Davis, C., and Gu, Y.: Dust radiative effects on atmospheric  
617 thermodynamics and tropical cyclogenesis over the Atlantic Ocean using  
618 WRF-Chem coupled with an AOD data assimilation system, *Atmos. Chem. Phys.*,  
619 17, 7917–7939, <https://doi.org/10.5194/acp-17-7917-2017>, 2017.
- 620 Chen, F. and Dudhia, J.: Coupling an advanced land surface-hydrology model with  
621 the Penn State-NCAR MM5 modeling system. Part I: Model implementation and

622 sensitivity, *Mon. Wea. Rev.*, 129, 569–585, doi:  
623 10.1175/1520-0493(2001)129<0569:CAALSH>2.0.CO;2, 2001.

624 Cheng, X., Sun, Z., Li, D., Xu, X., Jia, M., and Cheng, S.: Short-term aerosol  
625 radiative effects and their regional difference during heavy haze episodes in  
626 January 2013 in China, *Atmos. Environ.*, 165, 248–263,  
627 <http://dx.doi.org/10.1016/j.atmosenv.2017.06.040>, 2017.

628 Cheng, Y. F., Eichler, H., Wiedensohler, A., Heintzenberg, J., Zhang, Y. H., Hu, M.,  
629 Herrmann, H., Zeng, L.M., Liu, S., Gnauk, T., Brüggemann, E., and He, L.Y.,  
630 Mixing state of elemental carbon and non-light-absorbing aerosol components  
631 derived from in situ particle optical properties at Xinken in Pearl River Delta of  
632 China, *J. Geophys. Res.-Atmos.*, 111, D20204, doi: 10.1029/2005JD006929,  
633 2006.

634 Chou, M. D. and Suarez, M. J.: A solar radiation parameterization for atmospheric  
635 studies, Tech. Rep. NASA/TM-1999-104606, 15, Technical Report Series on  
636 Global Modeling and Data Assimilation NASA, 1999.

637 Ek, M. B., Mitchell, K. E., Lin, Y., Rogers, E., Grunmann, P., Koren, V., Gayno, G.,  
638 and Tarpley, J.D.: Implementation of Noah land surface model advances in the  
639 National Centers for Environmental Prediction operational mesoscale Eta model,  
640 *J. Geophys. Res.-Atmos.*, 108, 8851, doi:10.1029/2002JD003296, 2003.

641 Elser, M., Huang, R.-J., Wolf, R., Slowik, J. G., Wang, Q., Canonaco, F., Li, G.,  
642 Bozzetti, C., Daellenbach, K. R., Huang, Y., Zhang, R., Li, Z., Cao, J.,



643 Baltensperger, U., El-Haddad, I., and Prévôt, A. S. H.: New insights into PM<sub>2.5</sub>  
644 chemical composition and sources in two major cities in China during extreme  
645 haze events using aerosol mass spectrometry, *Atmos. Chem. Phys.*, 16, 3207–  
646 3225, <https://doi.org/10.5194/acp-16-3207-2016>, 2016.

647 Fan, J., Zhang, R., Tao, W. K., and Mhor, K. I.: Effects of aerosol optical properties  
648 on deep convective clouds and radiative forcing, *J. Geophys. Res.*, 113, D08209,  
649 doi:10.1029/2007JD009257, 2008.

650 Ghan, S. J., Liu, X., Easter, R. C., Zaveri, R., Rasch, P. J., Yoon, J.-H., Eaton, B.:  
651 Toward a Minimal Representation of Aerosols in Climate Models: Comparative  
652 Decomposition of Aerosol Direct, Semidirect, and Indirect Radiative Forcing, *J.*  
653 *Clim.*, 2012, 25, 6461-6476, doi: 10.1175/JCLI-D-11-00650.1, 2012.

654 Grell, G. A. and Baklanov, A.: Integrated modelling for forecasting weather and air  
655 quality: a call for fully coupled approaches, *Atmos. Environ.*, 45, 6845–6851,  
656 <https://doi.org/10.1016/j.atmosenv.2011.01.017>, 2011.

657 Grell, G. A. and Dévényi, D.: A generalized approach to parameterizing convection  
658 combining ensemble and data assimilation techniques, *Geophys. Res. Lett.*, 29,  
659 1693, doi: 10.1029/2002GL015311, 2002.

660 Grell, G., Freitas, S. R., Stuefer, M., and Fast, J.: Inclusion of biomass burning in  
661 WRF-Chem: impact of wildfires on weather forecasts, *Atmos. Chem. Phys.*, 11,  
662 5289-5303, <https://doi.org/10.5194/acp-11-5289-2011>, 2011.

663 Guo, J., Deng, M., Lee, S. S., Wang, F., Li, Z., Zhai, P., Liu, H., Lv, W., Yao, W., and

664 Li, X.,: Delaying precipitation and lightning by air pollution over the pearl river  
665 delta. Part I: observational analyses, *J. Geophys. Res.-Atmos*, 121, 6472–6488,  
666 doi:10.1002/2015JD023257, 2016.

667 Hansen, J., Sato, M., and Ruedy, R.: Radiative forcing and climate response, *J.*  
668 *Geophys. Res.-Atmos*, 102, 6831–6864, <https://doi.org/10.1029/96JD03436>,  
669 1997.

670 Hong, S.-Y., Noh, Y., and Dudhia, J.: A new vertical diffusion package with an  
671 explicit treatment of entrainment processes, *Mon. Weather Rev.*, 134, 2318–2341,  
672 doi:10.1175/Mwr3199.1, 2006.

673 Huang, C.-C., Chen, S.-H., Lin, Y.-C., Earl, K., Matsui, T., Lee, H.-H., Tsai, I.-C.,  
674 Chen, J.-P., and Cheng, C.-T.: Impacts of Dust–Radiation versus Dust–Cloud  
675 Interactions on the Development of a Modeled Mesoscale Convective System  
676 over North Africa, *Mon. Weather Rev.*, 47, 3301-3326.  
677 <https://doi.org/10.1175/MWR-D-18-0459.1>, 2019.

678 Huang, X., Ding, A., Liu, L., Liu, Q., Ding, K., Niu, X., Nie, W., Xu, Z., Chi, X.,  
679 Wang, M., Sun, J., Guo, W., and Fu, C.: Effects of aerosol–radiation interaction  
680 on precipitation during biomass-burning season in East China, *Atmos. Chem.*  
681 *Phys.*, 16, 10063 – 10082, <https://doi.org/10.5194/acp-16-10063-2016>, 2016.

682 Iacono, M. J., Delamere, J. S., Mlawer, E. J., Shephard, M. W., Clough, S. A.,  
683 Collins, W. D.: Radiative forcing by long-lived greenhouse gases: Calculations  
684 with the AER radiative transfer models, *J. Geophys. Res.-Atmos*, 113, D13, doi:

685 10.1029/2008JD009944, 2008.

686 Jiang, M., Feng, J., Li, Z., Sun, R., Hou, Y.-T., Zhu, Y., Wan, B., Guo, J., and Cribb,  
687 M.: Potential influences of neglecting aerosol effects on the NCEP GFS  
688 precipitation forecast, *Atmos. Chem. Phys.*, 17, 13967–13982,  
689 <https://doi.org/10.5194/acp-17-13967-2017>, 2017.

690 Kain, J. S.: The Kain-Fritsch convective parameterization: An update, *J. Appl.*  
691 *Meteorol.*, 43, 170–181, 2004.

692 Kaufman, Y. J., Tanre, D., and Boucher, O.: A satellite view of aerosols in the  
693 climate system, *Nature*, 419, 215-223, <http://dx.doi.org/10.1038/nature01091>,  
694 2002.

695 Liao, H., Chen, W. T., and Seinfeld, J. H.: Role of climate change in global  
696 predictions of future tropospheric ozone and aerosols, *J. Geophys. Res.*, 111,  
697 D12304, doi:10.1029/2005JD006852, 2006.

698 Liao, L., Lou, S. J., Fu, Y., Chang, W. J., and Liao, H.: Radiative forcing of aerosols  
699 and its impact on surface air temperature on the synoptic scale in eastern China,  
700 *Chinese J. Atmos. Sci.* (in Chinese), 39, 68–82, doi: doi:  
701 10.3878/j.issn.1006-9895.1402.13302, 2015.

702 Liu, X., Zhang, Y., Cheng, Y., Hu, M., and Han, T.: Aerosol hygroscopicity and its  
703 impact on atmospheric visibility and radiative forcing in Guangzhou during the  
704 2006 PRIDE-PRD campaign, *Atmos. Environ.* 60, 59–67,  
705 <https://doi.org/10.1016/j.atmosenv.2012.06.016>, 2012.

706 Mlawer, E. J., Taubman, S. J., Brown, P. D., Iacono, M. J. and Clough, S. A.:  
707 Radiative transfer for inhomogeneous atmospheres: RRTM, a validated  
708 correlated-k model for the longwave, *J. Geophys. Res.*, 102,  
709 doi:10.1029/97JD00237. 16663-16682, 1997.

710 Mulcahy, J. P., Walters, D. N., Bellouin, N., and Milton, S. F.: Impacts of increasing  
711 the aerosol complexity in the Met Office global numerical weather prediction  
712 model, *Atmos. Chem. Phys.*, 14, 4749–4778,  
713 <https://doi.org/10.5194/acp-14-4749-2014>, 2014.

714 Oreopoulos, L., Mlawer, E., Delamere, J., Shippert, T., Cole, J., Fomin, B., Iacono,  
715 M., Jin, Z., Li, J., Manners, J., Räisänen, P., Rose, F., Zhang, Y., Wilson, M. J.,  
716 and Rossow, W. B.: The Continual Intercomparison of Radiation Codes: Results  
717 from Phase I, *J. Geophys. Res.-Atmos.*, 117, D06118,  
718 <https://doi.org/10.1029/2011JD016821>, 2012.

719 Péré, J. C., Mallet, M., Pont, V., and Bessagnet B.: Impact of aerosol direct radiative  
720 forcing on the radiative budget, surface heat fluxes, and atmospheric dynamics  
721 during the heat wave of summer 2003 over western Europe: A modeling study, *J.*  
722 *Geophys. Res.*, 116, D23119, <https://doi.org/10.1029/2011JD016240>, 2011.

723 Pleim, J. E.: A Combined local and nonlocal closure model for the atmospheric  
724 boundary layer. Part I: Model description and testing, *J. Appl. Meteorol. Climat.*,  
725 46, 1383–1395, doi: 10.1175/JAM2539.1, 2007.

726 Quan, J., Tie, X., Zhang, Q., Liu, Q., Li, X., Gao, Y., and Zhao D.: (2014).

727 Characteristics of heavy aerosol pollution during the 2012–2013 winter in Beijing,  
728 China, *Atmos. Environ.*, **88**, 83–89,  
729 <https://doi.org/10.1016/j.atmosenv.2014.01.058>, 2014.

730 Ramanathan, V., Crutzen, P. J., Kiehl, J. T., and Rosenfeld, D.: Aerosols, Climate  
731 and the Hydrological Cycle, *Science*, **294**, 2119–2124, 2001.

732 Rémy, S., Benedetti, A., Bozzo, A., Haiden, T., Jones, L., Razinger, M., Flemming,  
733 J., Engelen, R. J., Peuch, V. H., and Thepaut, J. N.: Feedbacks of dust and  
734 boundary layer meteorology during a dust storm in the eastern Mediterranean,  
735 *Atmos. Chem. Phys.*, **15**, 12909–12933,  
736 <https://doi.org/10.5194/acp-15-12909-2015>, 2015.

737 Rodwell, M. J. and Jung T.: Understanding the local and global impacts of model  
738 physics changes: an aerosol example, *Q. J. Roy. Meteor. Soc.*, **134**, 1479–1497,  
739 <https://doi.org/10.1002/qj.298>, 2008.

740 Rogers, R. E., Deng, A. J., Stauffer, D. R., Gaudet, B. J., Jia, Y. Q., Soong, S. T., and  
741 Tanrikulu, S.: Application of the Weather Research and Forecasting Model for Air  
742 Quality Modeling in the San Francisco Bay Area, *J. Appl. Meteor. Clim.*, **52**,  
743 1953–1973, doi: 10.1175/JAMC-D-12-0280.1, 2013.

744 Ruiz-Arias, J. A., Dudhia, J., and Gueymard, C. A.: A simple parameterization of the  
745 short-wave aerosol optical properties for surface direct and diffuse irradiances  
746 assessment in a numerical weather model, *Geosci. Model Dev.*, **7**, 1159–1174,  
747 doi:10.5194/gmd-7-1159-2014, 2014.

748 Sekiguchi, A., Shimadera, H., and Kondo, A.: 2018, Impact of Aerosol Direct Effect  
749 on Wintertime PM<sub>2.5</sub> Simulated by an Online Coupled Meteorology-Air Quality  
750 Model over East Asia, *Aerosol and Air Quality Research*, 18: 1068–1079, doi:  
751 10.4209/aaqr.2016.06.0282, 2018.

752 Thompson, G., Field, P. R., Rasmussen, R. M., and Hall, W. D.: Explicit forecasts of  
753 winter precipitation using an improved bulk microphysics scheme. Part II:  
754 Implementation of a new snow parameterization, *Mon. Weather Rev.*, 136, 5095–  
755 5115, <https://doi.org/10.1175/2008MWR2387.1>, 2008.

756 Toll, V., Gleeson, E., Nielsen, K.P., Männik, A., Mašek, J., Rontu, L., and Post, P.:  
757 Impacts of the direct radiative effect of aerosols in numerical weather prediction  
758 over Europe using the ALADIN-HIRLAM NWP system, *Atmos. Res.*, 172-173,  
759 163-173, <https://doi.org/10.1016/j.atmosres.2016.01.003>, 2016.

760 Toll, V., Reis, K., Ots, R., Kaasik, M., Männik, A., Prank, M., Sofiev, M.: SILAM  
761 and MACC reanalysis aerosol data used for simulating the aerosol direct radiative  
762 effect with the NWP model HARMONIE for summer 2010 wildfire case in  
763 Russia, *Atmos. Environ.*, 121, 75-85,  
764 <https://doi.org/10.1016/j.atmosenv.2015.06.007>, 2015.

765 Wang, H., Shi, G. Y., Zhang, X. Y., Gong, S. L., Tan, S. C., Chen, B., Che, H. Z., and  
766 Li, T.: Mesoscale modelling study of the interactions between aerosols and PBL  
767 meteorology during a haze episode in China Jing–Jin–Ji and its near surrounding  
768 region – Part 2: Aerosols' radiative feedback effects, *Atmos. Chem. Phys.*, 15,

769 3277-3287, <https://doi.org/10.5194/acp-15-3277-2015>, 2015b.

770 Wang, H., Xue, M., Zhang, X. Y., Liu, H. L., Zhou, C. H., Tan, S. C., Che, H. Z.,  
771 Chen, B., and Li, T.: Mesoscale modeling study of the interactions between  
772 aerosols and PBL meteorology during a haze episode in Jing–Jin–Ji (China) and  
773 its nearby surrounding region – Part 1: Aerosol distributions and meteorological  
774 features, *Atmos. Chem. Phys.*, 15, 3257–3275,  
775 <https://doi.org/10.5194/acp-15-3257-2015>, 2015a.

776 Wang, J., Wang, S., Jiang, J., Ding, A., Zheng, M., Zhao, B., Wong, D. C., Zhou, W.,  
777 Zheng, G., Wang, L., Pleim, J. E. and Hao, J.: Impact of aerosol–meteorology  
778 interactions on fine particle pollution during China's severe haze episode in  
779 January 2013, *Environ. Res. Lett.*, 9, 094002, doi:10.1088/1748-9326/9/9/094002,  
780 2014.

781 Wang, X., He, X., Miao, S., Dou, Y.: Numerical simulation of the influence of  
782 aerosol radiation effect on urban boundary layer, *Sci. China Earth Sci.*, 61, 1844–  
783 1858, <https://doi.org/10.1007/s11430-018-9260-0>, 2018.

784 Yang, X., Zhao, C., Zhou, L., Wang, Y., Liu, X.: Distinct impact of different types of  
785 aerosols on surface solar radiation in China, *J. Geophys. Res.-Atmos.*, 121,  
786 6459-6471, doi: 10.1002/2016JD024938, 2017b.

787 Yang, Y. and Ren, R. C.: On the contrasting decadal changes of diurnal surface  
788 temperature range between the Tibetan Plateau and southeastern China during the  
789 1980s–2000s, *Adv. Atmos. Sci.*, 34, 181–198, doi: 10.1007/s00376-016-6077-z,

790 2017a.

791 Yu, H., Kaufman, Y. J., Chin, M., Feingold, G., Remer, L. A., Anderson, T. L.,  
792 Balkanski, Y., Bellouin, N., Boucher, O., Christopher, S., DeCola, P., Kahn, R.,  
793 Koch, D., Loeb, N., Reddy, M. S., Schulz, M., Takemura, T., and Zhou, M.: A  
794 review of measurement-based assessments of the aerosol direct radiative effect  
795 and forcing, *Atmos. Chem. Phys.*, 6, 613-666,  
796 <https://doi.org/10.5194/acp-6-613-2006>, 2006.

797 Zaveri, R. A. and Peters, L. K.: A new lumped structure photochemical mechanism  
798 for large-scale applications, *J. Geophys. Res.*, 104, 30387–30415,  
799 <https://doi.org/10.1029/1999JD900876>, 1999.

800 Zhai, S., Jacob, D. J., Wang, X., Shen, L., Li, K., Zhang, Y., Gui, K., Zhao, T., and  
801 Liao, H.: Fine particulate matter (PM<sub>2.5</sub>) trends in China, 2013–2018: separating  
802 contributions from anthropogenic emissions and meteorology, *Atmos. Chem.*  
803 *Phys.*, 19, 11031-11041, <https://doi.org/10.5194/acp-19-11031-2019>, 2019.

804 Zhang, B., Wang, Y., and Hao, J.: Simulating aerosol–radiation–cloud feedbacks on  
805 meteorology and air quality over eastern China under severe haze conditions in  
806 winter, *Atmos. Chem. Phys.*, 15, 2387-2404,  
807 <https://doi.org/10.5194/acp-15-2387-2015>, 2015.

808 Zhang, Q., Ma, Q., Zhao, B., Liu, X., Wang, Y., Jia, B., and Zhang, X.: Winter haze  
809 over North China Plain from 2009 to 2016: Influence of emission and  
810 meteorology, *Environ. Pollut.*, 242, 1308–1318.



811 doi:10.1016/j.envpol.2018.08.019, 2018.

812 Zhang, Q., Quan, J., Tie, X., Li, X., Liu, Q., Gao, Y., and Zhao, D. L.: Effects of  
813 meteorology and secondary particle formation on visibility during heavy haze  
814 events in Beijing, China, *Sci. Total Environ.*, 502, 578–584,  
815 <https://doi.org/10.1016/j.scitotenv.2014.09.079>, 2015.

816 Zhang, Y., Wen, X.-Y., and Jang, C.-J.: Simulating  
817 chemistry-aerosol-cloud-radiation-climate feedbacks over the continental U.S.  
818 using the online-coupled Weather Research Forecasting Model with chemistry  
819 (WRF/Chem), *Atmos. Environ.* 44, 3568–3582,  
820 <https://doi.org/10.1016/j.atmosenv.2010.05.056>, 2010.

821 Zhang, Y.-Z, Miao, S.-G., Dai, Y.-J., Liu, Y.-H., Numerical simulation of  
822 characteristics of summer clear day boundary layer in Beijing and the impact of  
823 urban underlying surface on sea breeze (in Chinese), *Chin J. Geophys*, 56,  
824 2558–2573, 2013.

825 Zhao, X., Li, Z., Xu, J.: Modification and performance tests of visibility  
826 parameterizations for haze days, *Environ. Sci.*, 40, 1688-1696 (in Chinese), 2019.

827 Zheng, Y., Che, H., Xia, X., Wang, Y., Wang, H., Wu, Y., Tao, J., Zhao, H., An, J.,  
828 Li, L., Gui, K., Sun, T., Li, X., Sheng, Z., Liu, C., Yang, X., Liang, Y., Zhang, L.,  
829 Liu, C., Kuang, X., Luo, S., You, Y., and Zhang, X.: Five-year observation of  
830 aerosol optical properties and its radiative effects to planetary boundary layer  
831 during air pollution episodes in North China: Intercomparison of a plain site and

832 a mountainous site in Beijing, *Sci. Total Environ.*, 674, 140–158.  
833 <https://doi.org/10.1016/j.scitotenv.2019.03.418>, 2019.

834 Table 1. The variables, sources, numbers of sites in the domain/NCP and the  
 835 frequency of chemical and meteorological observations.

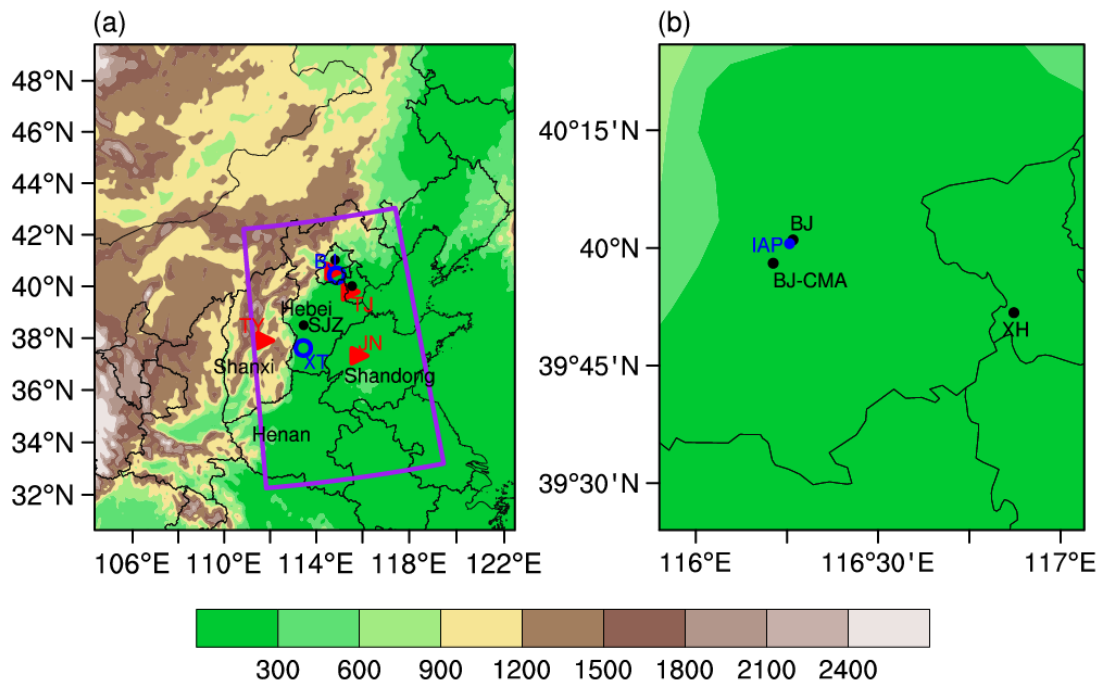
Variables	Source of observation	Numbers of sites over the domain/NCP	Frequency	locations
AOD	AERONET	3/3	hourly	black dots in Fig. 1b
AOD	IAP station	1/1	hourly	blue dot in Fig. 1b
AOD	MODIS	/	daily	Fig. 2f-j and Fig. 2p-t
aerosol extinction coefficient	CALIPSO	/	daily	black paths in Fig.3a-d
PM <sub>2.5</sub>	China National Environmental Monitoring Centre	813/332	hourly	dots in Fig. 5a
radiation	China Meteorological Administration	4/4	hourly	triangles in Fig. 1a
radiation	IAP station	1/1	hourly	triangles in Fig. 1a
2-m temperature	China Meteorological Administration	1157/534	hourly	dots in Fig. 11a
wind at 10m	China Meteorological Administration	1157/534	hourly	dots in Fig. 11a
atmospheric wind	China Meteorological Administration	2/2	0800LT, 2000LT	circles in Fig. 1a

836

837 Table 2. Mean bias of downward SW radiation at surface ( $W m^{-2}$ ) and Net radiation  
838 at surface ( $W m^{-2}$ ) from NoAero and Aero relative to observation during daytime  
839 (averaged 0800 to 1800 LT) and nighttime (averaged 1900 to 0700 LT), averaged  
840 from 6<sup>th</sup> to 11<sup>th</sup> Dec. 2015 at Beijing, Tianjin, Taiyuan and Jinan respectively.

841

Station	SW radiation		Net radiation			
	Daytime		Daytime		Nighttime	
	NoAero	Aero	NoAero	Aero	NoAero	Aero
Beijing	149.4	38.0	102.2	15.0	-33.6	-33.2
Tianjin	115.5	70.9	72.2	36.4	-27.1	-26.4
Taiyuan	155.0	118.3	66.9	43.2	-33.6	-33.3
Jinan	149.1	97.7	81.2	45.3	-30.3	-29.3



842

843 Figure 1. (a) The model domain and the terrain height (shadings, m). Purple box

844 denotes the NCP, triangles are the observational sites of radiation (BJ: Beijing, TJ:

845 Tianjin, TY: Taiyuan and JN: Jinan), circles are sites of sounding observation (BJ:

846 Beijing and XT: Xingtai), dots denote the major cities for validation of PM<sub>2.5</sub> (BJ:

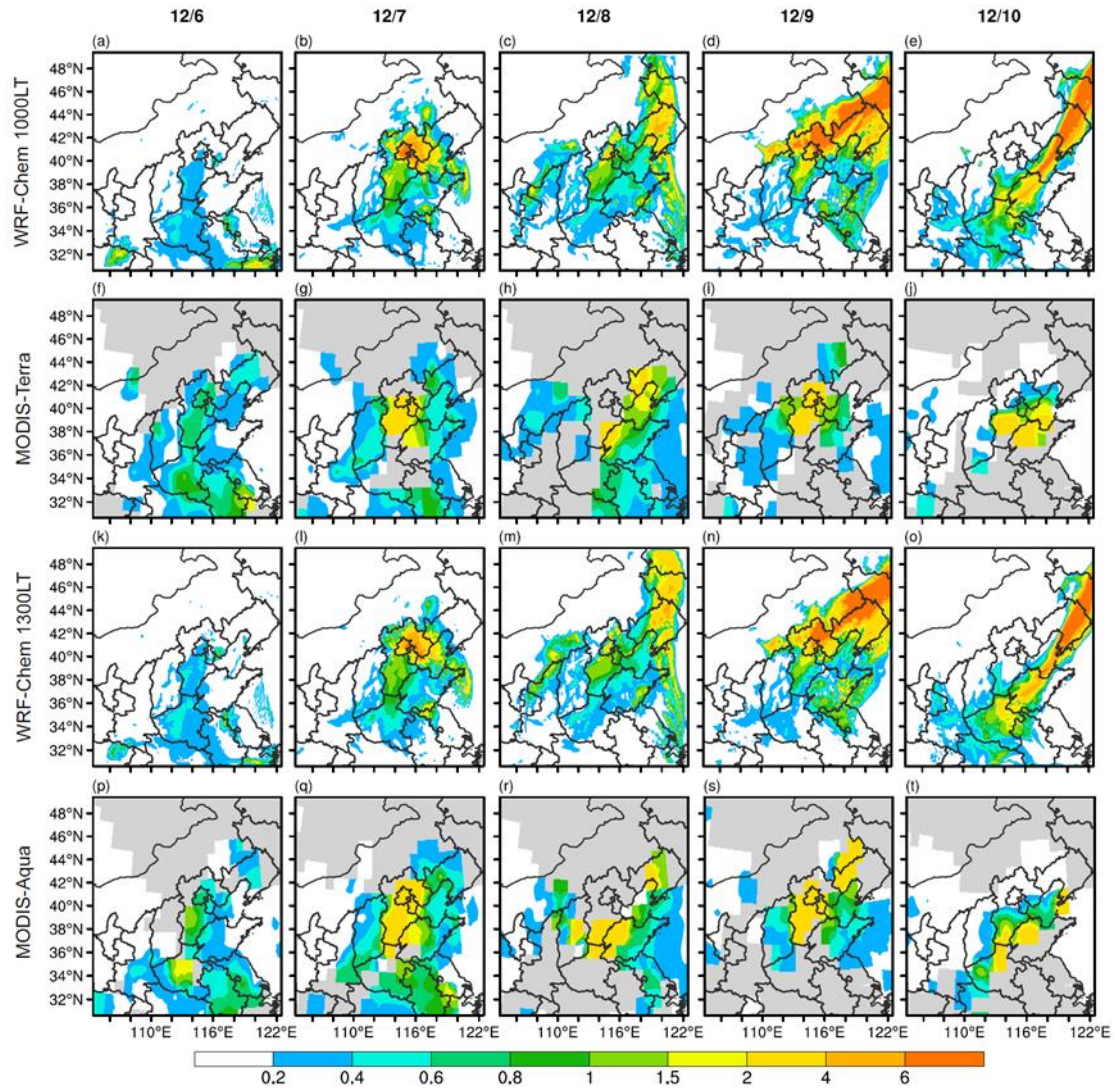
847 Beijing, SJZ: Shijiazhuang and TJ: Tianjin). Names of provinces are also added

848 (Hebei, Shanxi, Shandong and Henan). (b) The observational sites of AOD,

849 including AERONET sites (black dots, BJ: Beijing, BJ-CMA: Beijing-CMA and XH:

850 Xianghe) and IAP in-situ (blue dot) site.

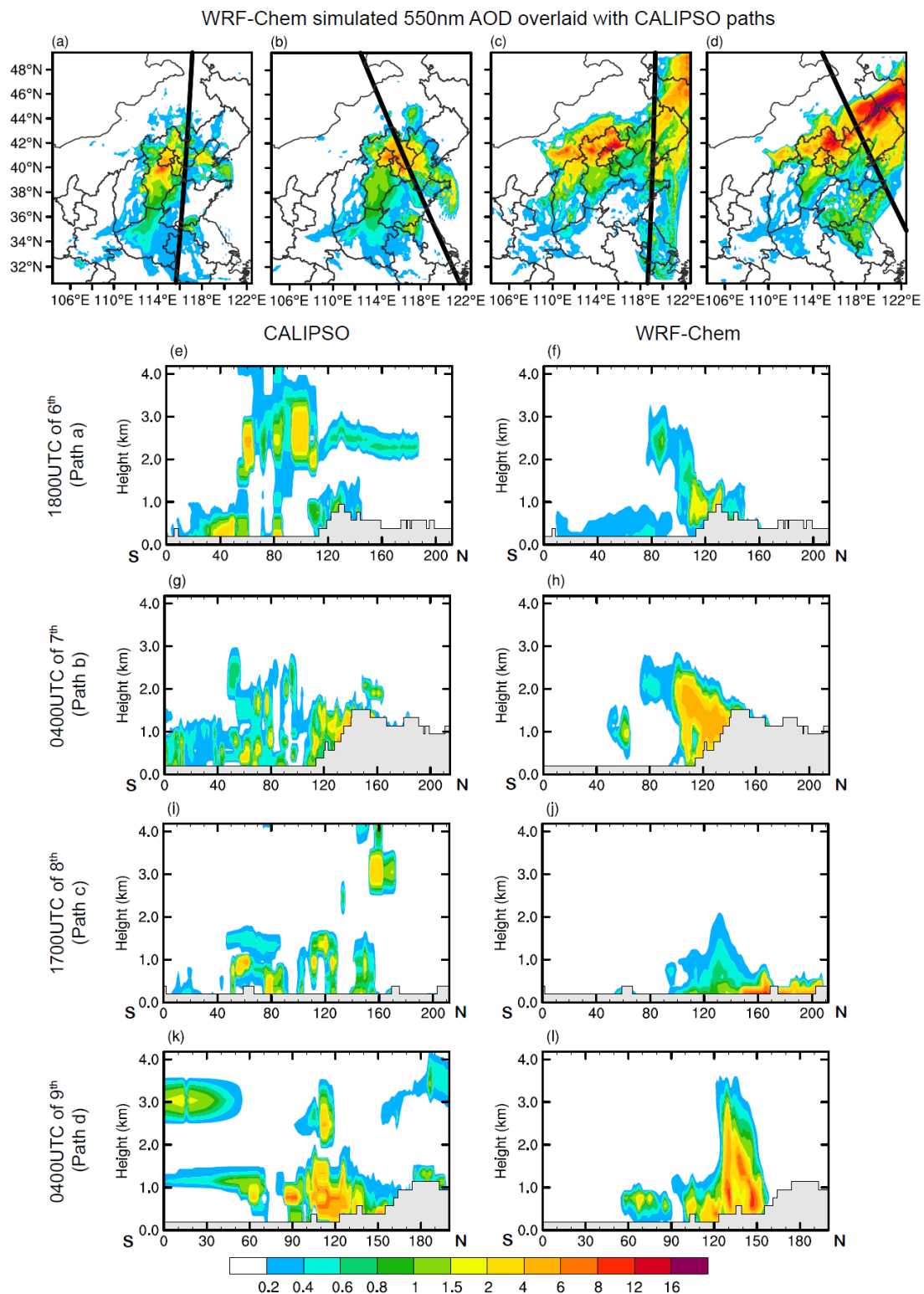
851



852

853 Figure 2. The WRF-Chem simulated and MODIS observed spatial distribution of  
 854 AOD on 6th-10th December (from left to right). The first (a-e) and third rows (k-o)  
 855 are WRF-Chem simulations at 1000LT and 1300LT (MODIS path times)  
 856 respectively. The second (f-j) and fourth (p-t) rows are MODIS Terra and Aqua  
 857 observations, respectively. Gray areas in (f-j) and (p-t) denote the missing values.

858



859

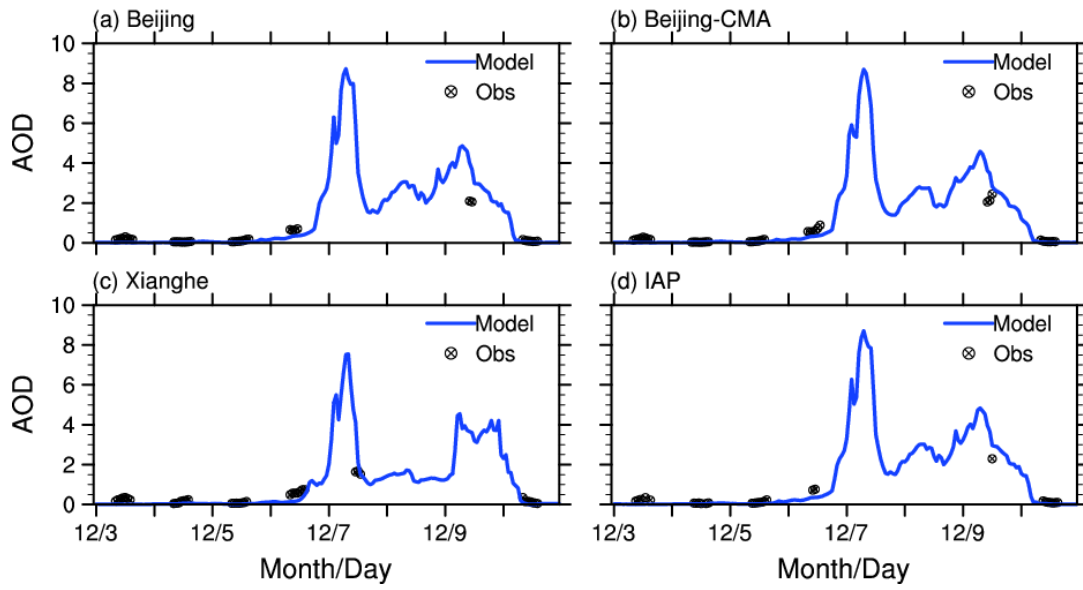
860 Figure 3. The WRF-Chem simulated 550nm AOD (shadings) on (a)1800UTC of 6<sup>th</sup>,  
 861 (b) 0400UTC of 7<sup>th</sup>, (c)1700UTC of 8<sup>th</sup>, (d) 0400UTC of 9<sup>th</sup> December overlaid with  
 862 CALIPSO paths (black thick solid). (e-l) denote the corresponding vertical

863 distributions of aerosol extinction coefficient at 550nm from (e, g, i, k) CALIPSO and

864 (f, h, j, l) model simulations. Gray areas in (e-l) denote the terrain.

865





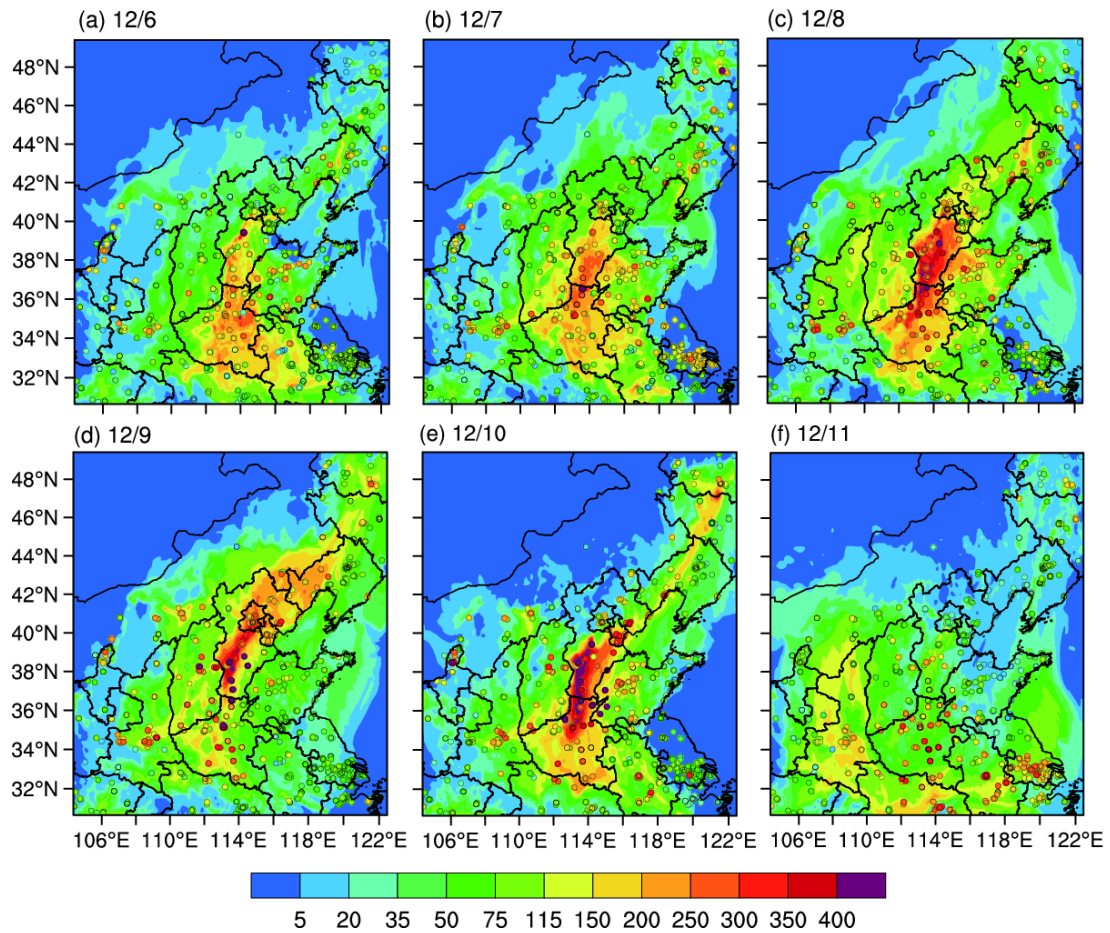
866

867 Figure 4. Temporal variation of observed (black dots) and simulated (blue) AOD at

868 550nm during 3<sup>rd</sup>-10<sup>th</sup> Dec. (LT) at (a) Beijing, (b) Beijing-CMA, (c) Xianghe and (d)

869 IAP, AOD observations are from (a-c) AERONET and (d) IAP in-situ site.

870



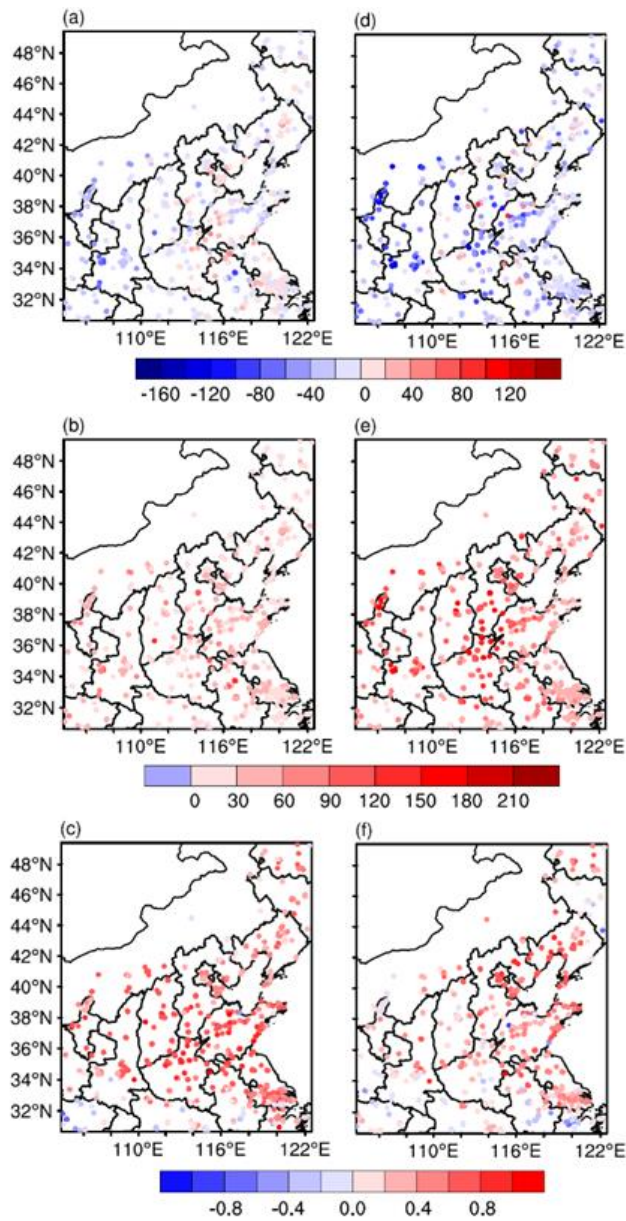
871

872 Figure 5. Observed (colored dots) and WRF-Chem simulated (shadings) spatial

873 distribution of PM<sub>2.5</sub> concentrations ( $\mu\text{g m}^{-3}$ ) on 0800LT of (a) 6<sup>th</sup>, (b) 7<sup>th</sup>, (c) 8<sup>th</sup>, (d)

874 9<sup>th</sup>, (e) 10<sup>th</sup> and (f) 11<sup>th</sup> Dec. respectively.

875



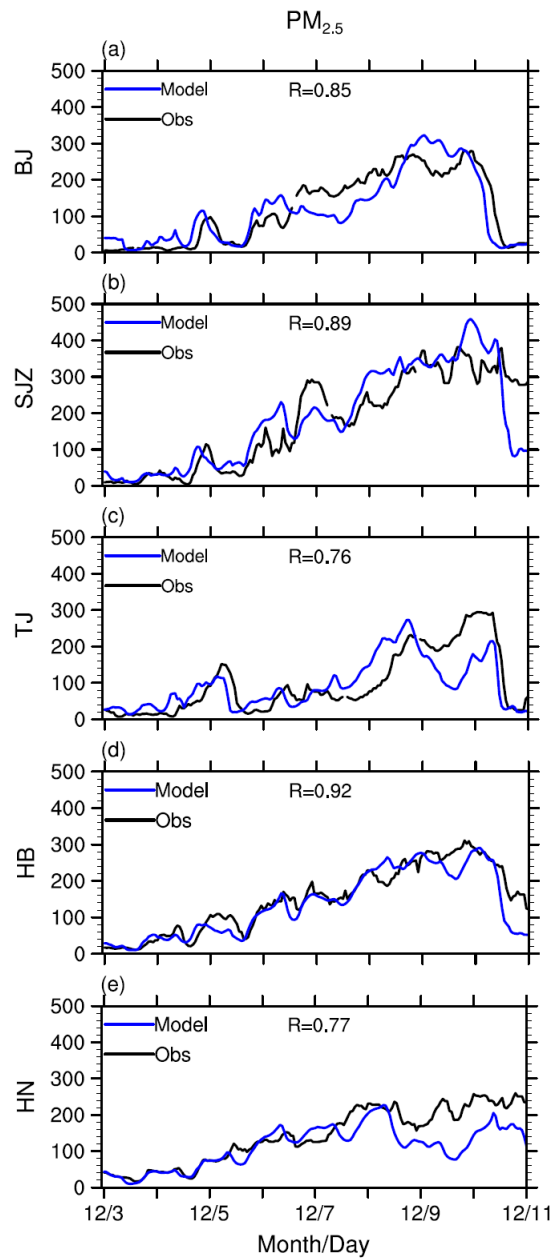
876

877 Figure 6. The (a, d) bias ( $\mu\text{g m}^{-3}$ ), (b, e) RMSE ( $\mu\text{g m}^{-3}$ ), and (c, f) correlation

878 coefficient (1) averaged (a-c) during clean period (3th to 5th Dec.) and (d-f) the

879 polluted period (6th to 10th December).

880



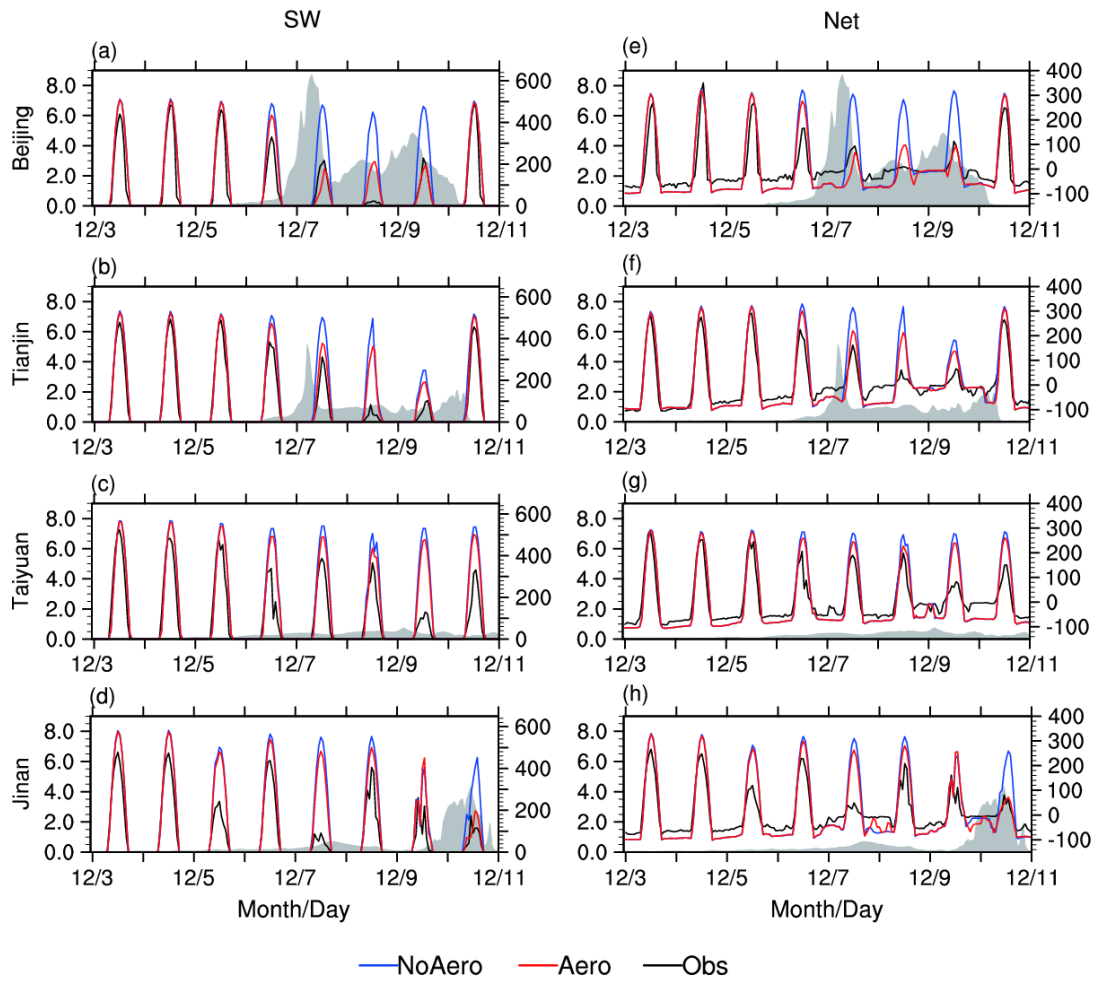
881

882 Figure 7. Observed (black) and WRF-Chem simulated (blue) temporal variation of

883  $PM_{2.5}$  ( $\mu g m^{-3}$ ) at three major cities (a) Beijing (BJ), (b) Shijiazhuang (SJZ)

884 (c) Tianjin (TJ) and two provinces (d) Hebei (HB) and (e) Henan (HN).

885



886

—NoAero —Aero —Obs

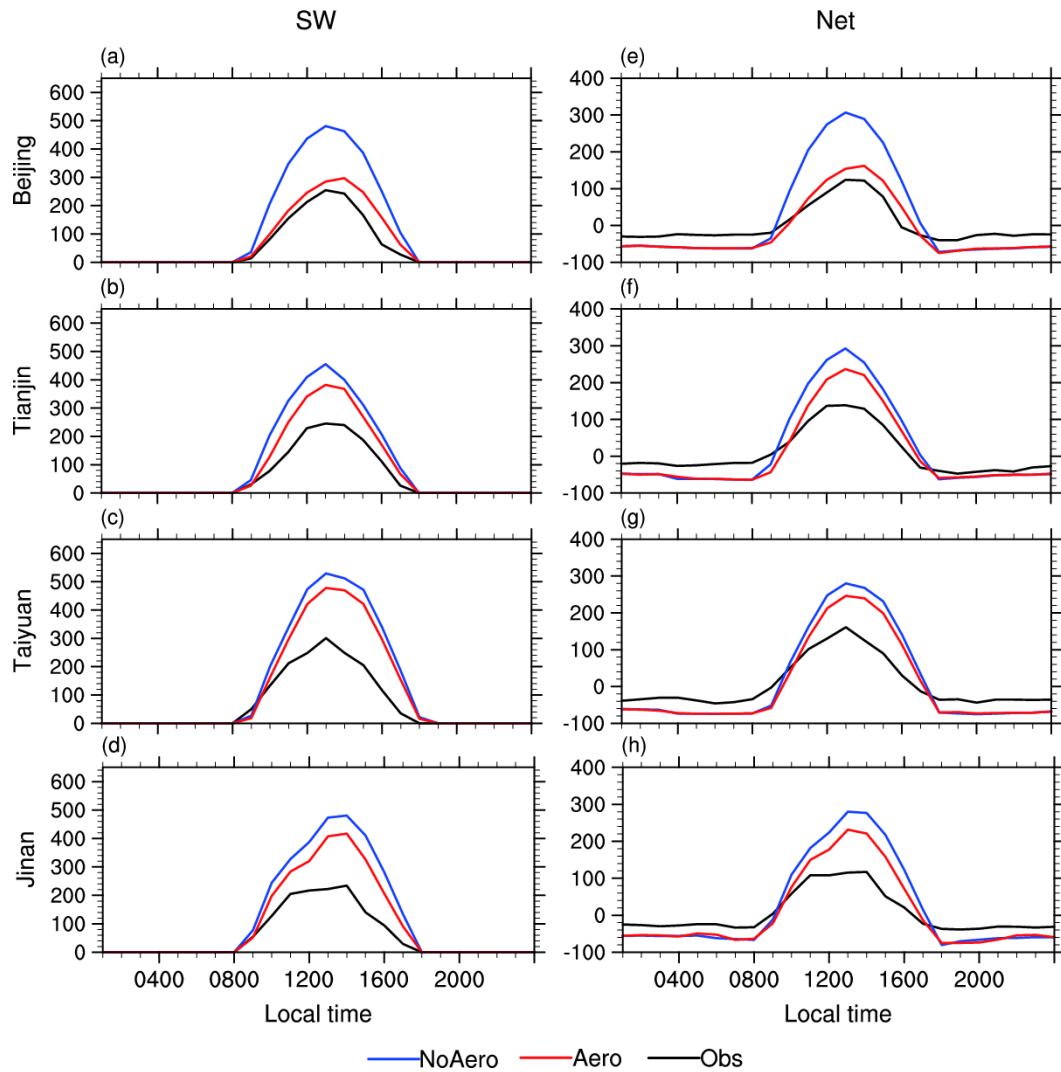
887 Figure 8. (a–d) observed (black) and WRF simulated (NoAero: blue, Aero: red)

888 temporal variation of downward shortwave radiation at surface ( $\text{W m}^{-2}$ , right axis)

889 at (a) Beijing, (b) Tianjin, (c) Taiyuan and (d) Jinan, respectively. The grey areas

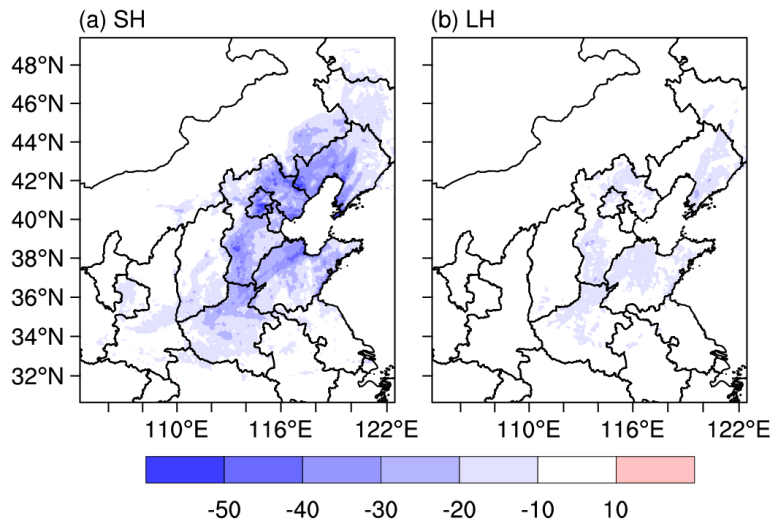
890 indicate the simulated AOD (left axis) by WRF-Chem. (e–h) are same with (a–d),

891 but for net radiation at surface ( $\text{W m}^{-2}$ ).



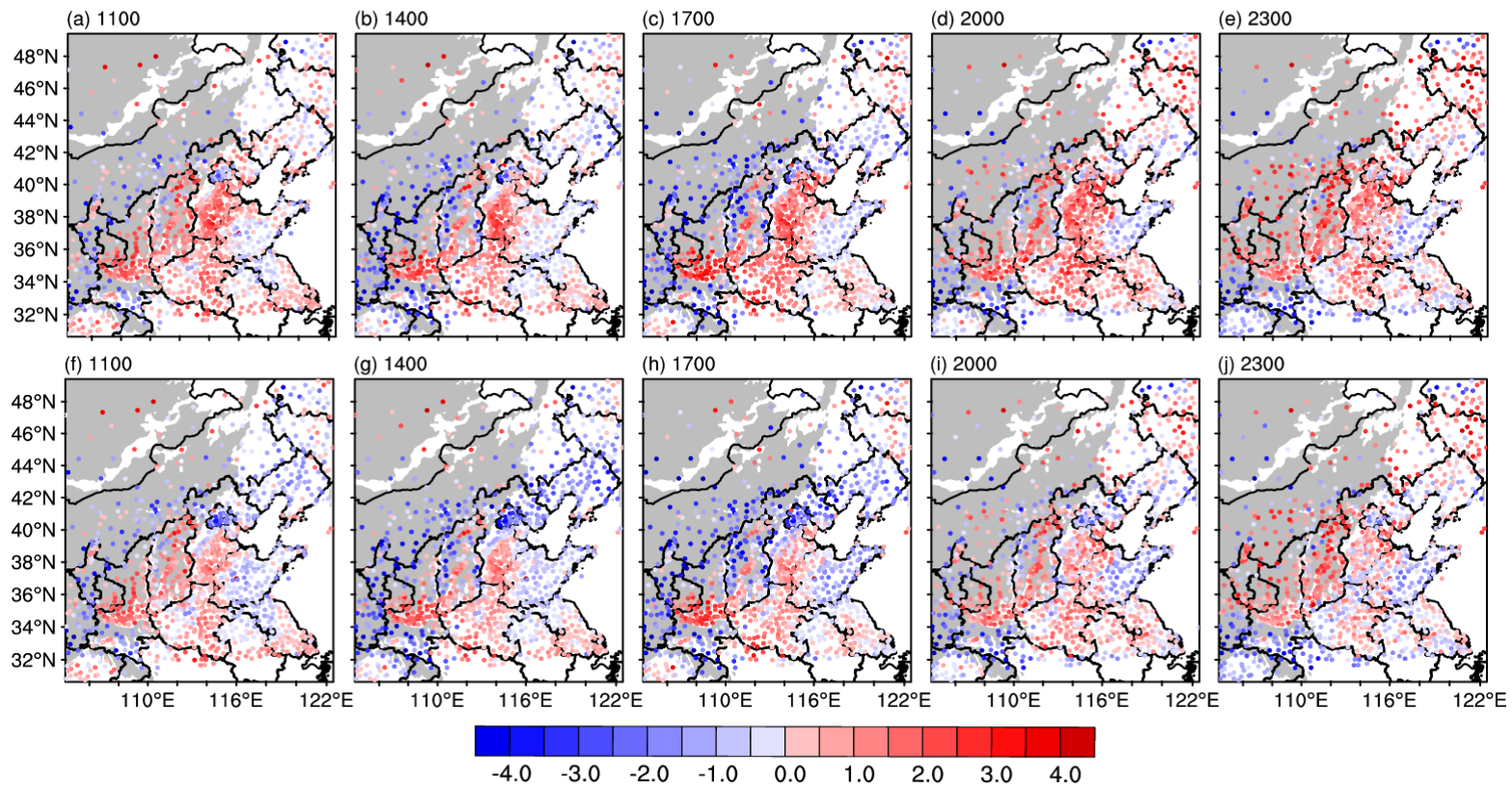
892

893 Figure 9. (a–d) observed (black) and simulated (NoAero: blue, Aero: red) diurnal  
 894 cycles of downward shortwave radiation at surface ( $W m^{-2}$ ) averaged from 6<sup>th</sup> to 10<sup>th</sup>  
 895 Dec. 2015 at (a) Beijing, (b) Tianjin, (c) Taiyuan and (d) Jinan, respectively. (e–h)  
 896 are same with (a–d), but for net radiation at surface ( $W m^{-2}$ ).



897

898 Figure 10. The differences (Aero minus NoAero) of (a) surface sensible heat flux  
 899 and (b) surface latent heat flux ( $\text{W m}^{-2}$ , upward is positive) at 1300LT averaged  
 900 from 6th to 10th Dec. 2015.

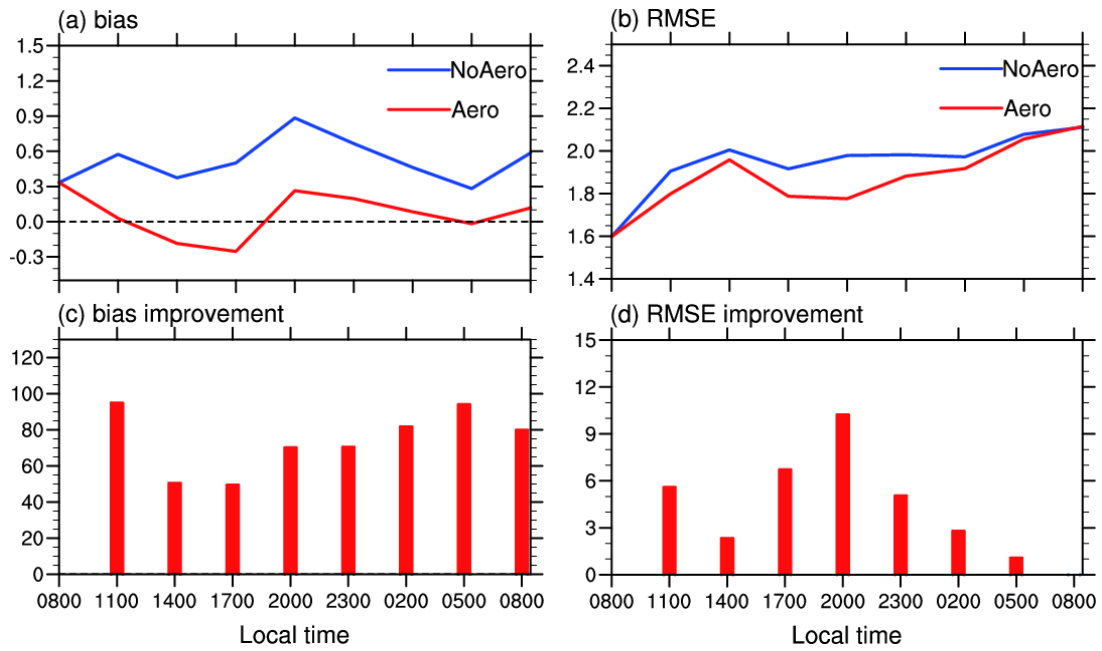


901

902 Figure 11. The bias of 2-m temperature ( $^{\circ}\text{C}$ ) at (a) 1100, (b) 1400, (c) 1700, (d) 2000 and (e) 2300 LT in NoAero averaged from 6th to 10th Dec.

903 2015, (f–j) are same with (a–e), but for Aero. The grey areas denote the areas of terrain height above 1000m.





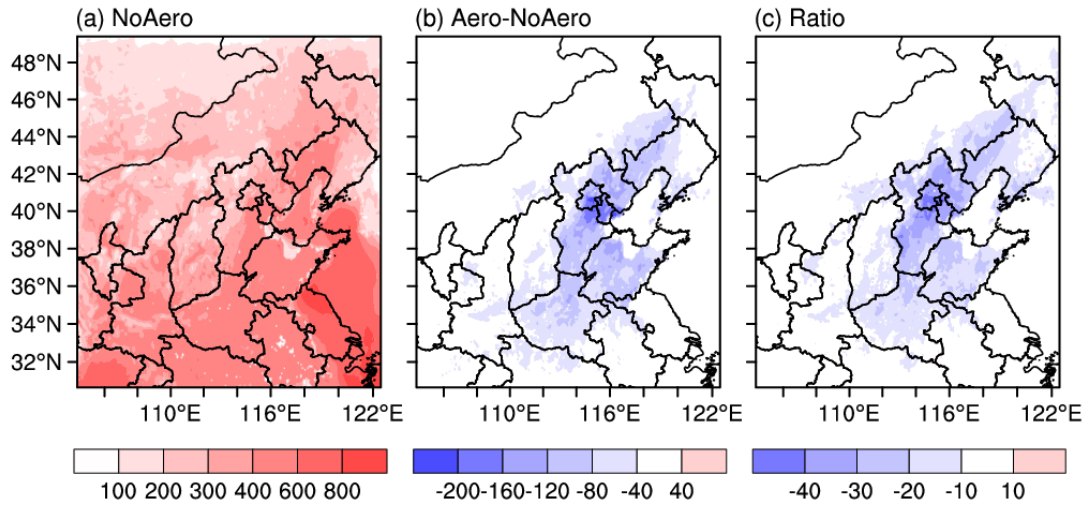
904

905 Figure 12. Area-averaged (a) bias and (b) RMSE of simulated 2-m temperature (°C )

906 in NoAero (blue) and Aero (red) over NCP area (defined in Fig. 1a), averaged from

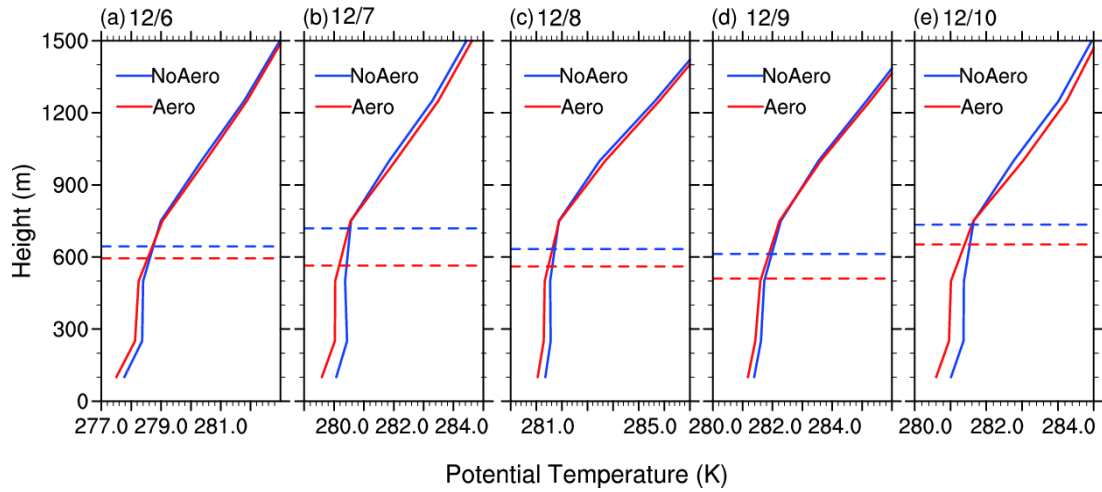
907 6<sup>th</sup> to 10<sup>th</sup> Dec. 2015, and the mean improvement (%) of (c) absolute value of bias

908 and (d) RMSE in Aero relative to NoAero.



909

910 Figure 13. Daytime mean PBLH (m) in NoAero, (b) the difference between Aero  
 911 and NoAero (Aero minus NoAero) and (c) the ratio of changes (%) averaged during  
 912 6<sup>th</sup> to 10<sup>th</sup> Dec. 2015.



913

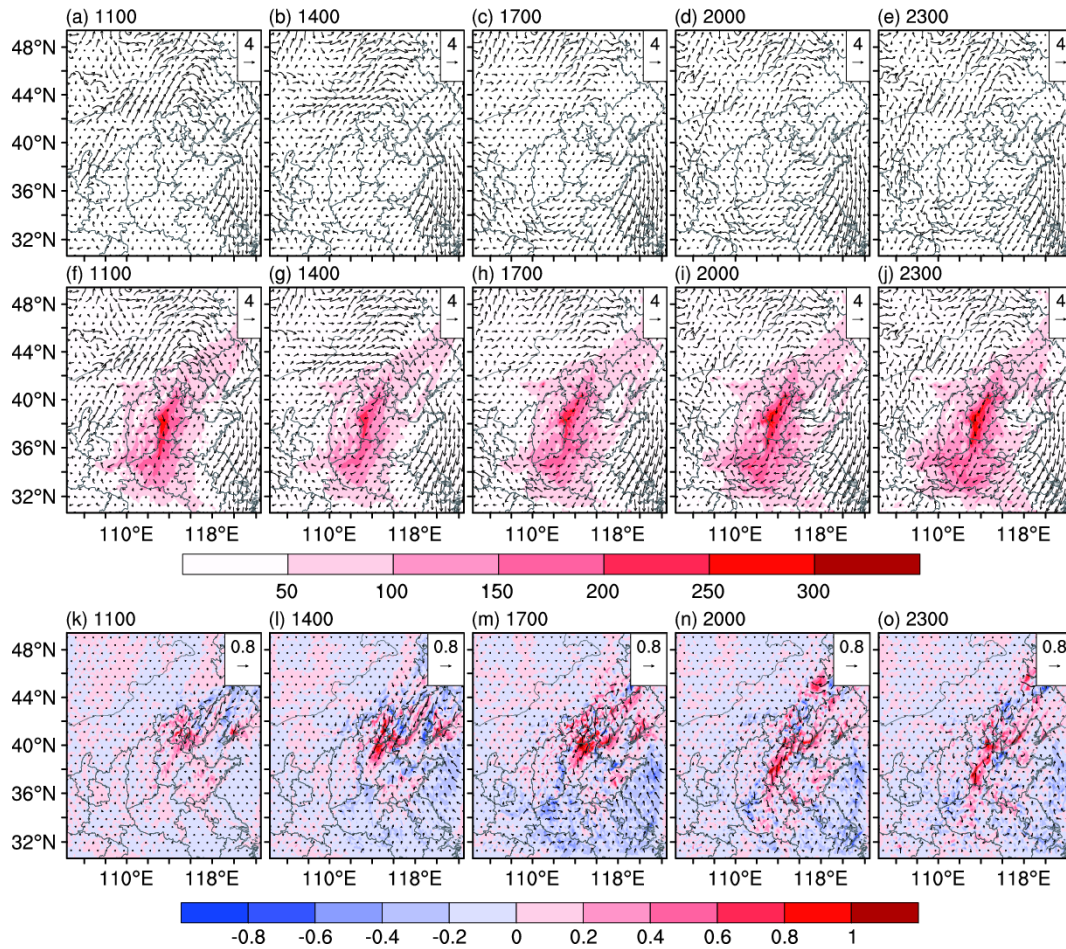
Potential Temperature (K)

914 Figure 14. NCP (defined in Fig. 1a) area-averaged vertical profiles of potential

915 temperature (K, solid) and planetary boundary-layer height (m, dash) in NoAero

916 (blue) and Aero (red) at 1400 LT of (a) 6<sup>th</sup>, (b) 7<sup>th</sup>, (c) 8<sup>th</sup>, (d) 9<sup>th</sup> and (e) 10<sup>th</sup> Dec.

917 2015.



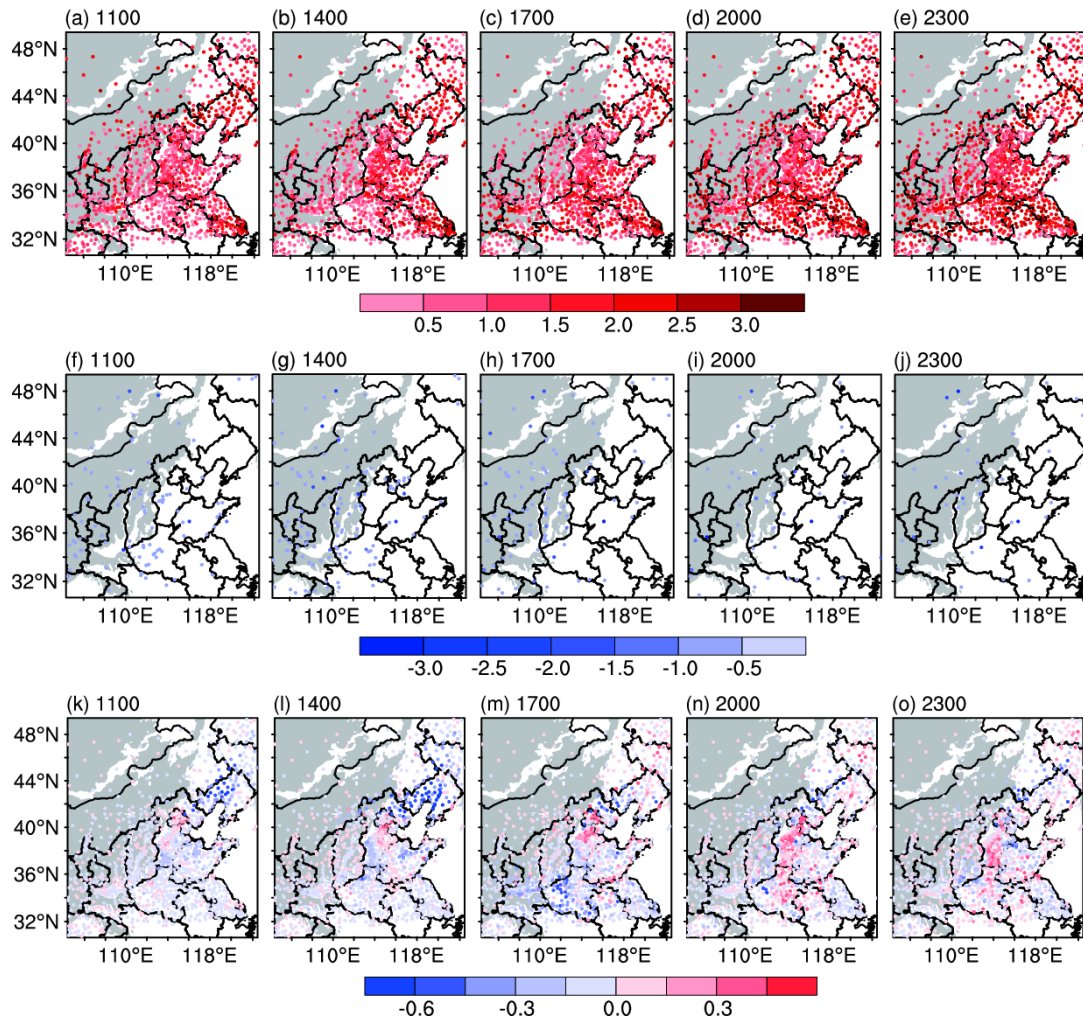
918

919 Figure 15. The 10m wind (vector) at 1100, 1400, 1700, 2000 and 2300 LT in (a–e)

920 NoAero and (f–j) Aero averaged during 6<sup>th</sup> to 10<sup>th</sup> Dec. 2015, shadings in (f–j) are

921 simulated PM<sub>2.5</sub> concentrations ( $\mu\text{g m}^{-3}$ ). (k–o) the difference of 10m wind (vector)

922 and wind speed (shadings) between Aero and NoAero (Aero minus NoAero).



923

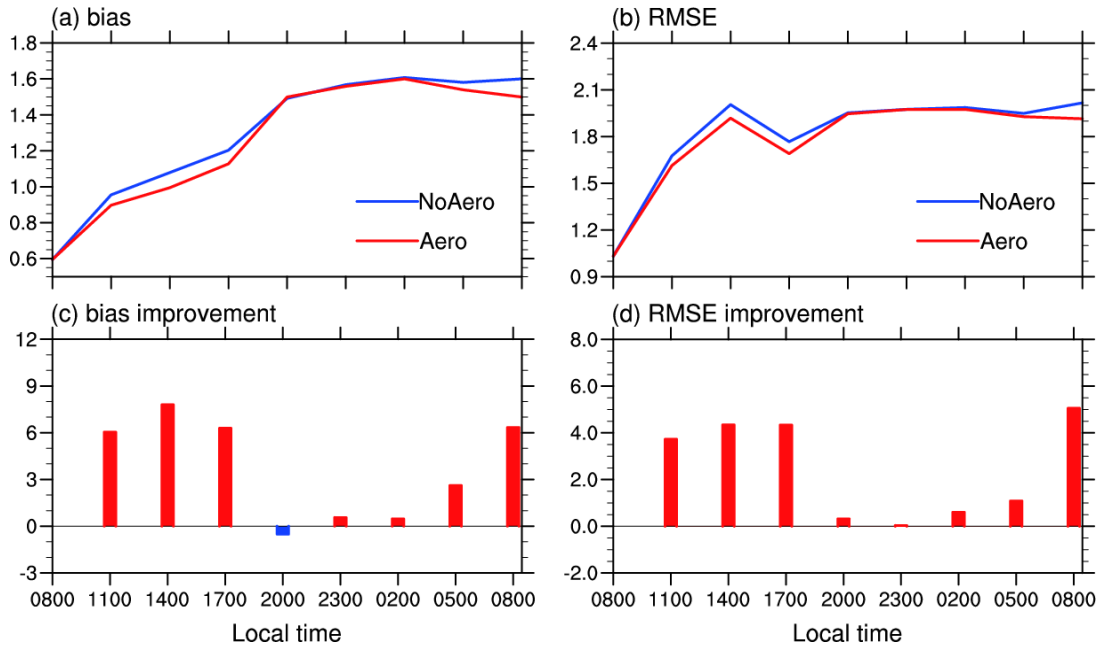
924 Figure 16. The bias of 10m wind speed ( $\text{m s}^{-1}$ ) at 1100, 1400, 1700, 2000 and 2300

925 LT for (a–e) overestimated sites and (f–j) underestimated sites in NoAero averaged

926 during 6<sup>th</sup> to 10<sup>th</sup> Dec. 2015. (k–o) the difference of absolute value of bias ( $\text{m s}^{-1}$ )

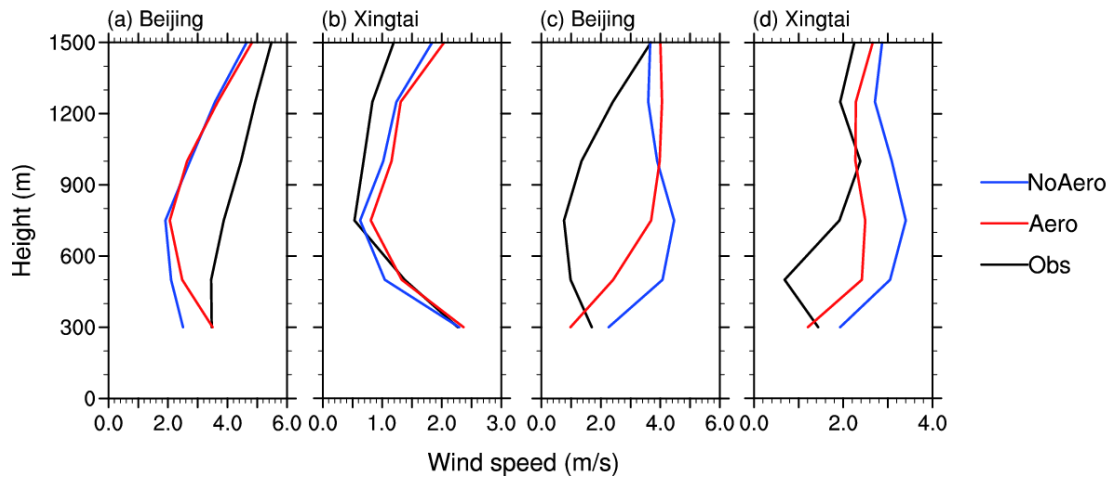
927 between Aero and NoAero (Aero minus NoAero). The grey areas denote the areas of

928 terrain height above 1000m.



929

930 Figure 17. Same with Fig.12, but for wind speed at 10m ( $\text{m s}^{-1}$ ).

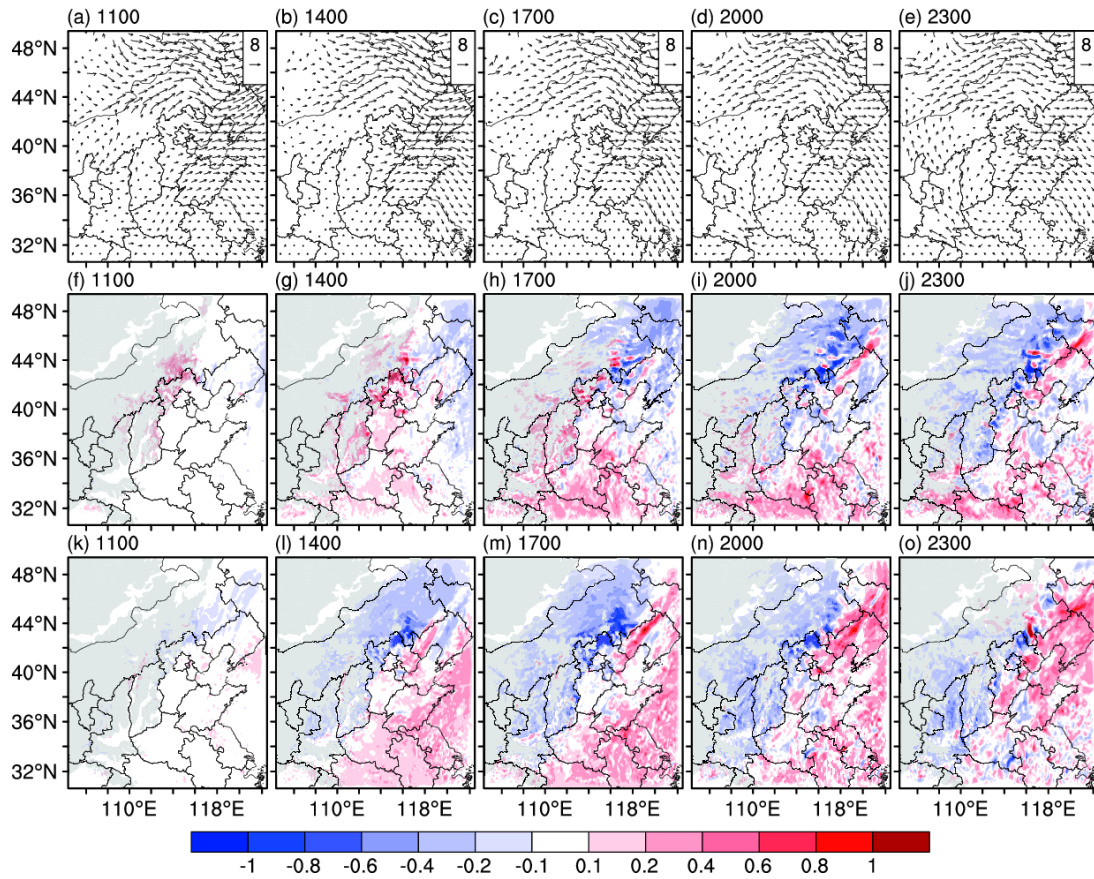


931

932 Figure 18. (a–b) Observed (black) and simulated (NoAero: blue, Aero: red) vertical

933 profiles of atmospheric wind speed ( $\text{m s}^{-1}$ ) at (a) Beijing and (b) Xingtai at 0800LT

934 averaged from 6<sup>th</sup> to 10<sup>th</sup> Dec., (c–d) are same with (a–b), but at 2000LT.



935

936 Figure 19. The wind at 850hPa (vector) at 1100, 1400, 1700, 2000 and 2300 LT in  
 937 NoAero averaged during 6<sup>th</sup> to 10<sup>th</sup> Dec. 2015. The difference of (f–j) U and (k–o) V  
 938 wind speed between Aero and NoAero (Aero minus NoAero). The grey areas denote  
 939 the areas of terrain height above 1000m.